공학박사학위논문

A Study on Transfer Function Design for Direct Volume Rendering

직접 볼륨 렌더링의 전이 함수 설계에 관한 연구

2017년 2월

서울대학교 대학원

전기 • 컴퓨터공학부

윤 지 혜

A Study on Transfer Function Design for Direct Volume Rendering

직접 볼륨 렌더링의 전이 함수 설계에 관한 연구

지도교수 신 영 길

이 논문을 공학박사 학위논문으로 제출함

2016년 10월

서울대학교 대학원

전기 • 컴퓨터공학부

윤 지 혜

윤지혜의 공학박사 학위논문을 인준함

2016년 12월

위 원 장 김 명 수 (인)

부 위 원 장 신 영 길 (인)

위 원 서 진 욱 (인)

위 원 김 보 형 (인)

위 원 이 정 진 (인)

Abstract

A Study on Transfer Function Design for Direct Volume Rendering

Jihye Yun
School of Computer Science and Engineering
The Graduate School
Seoul National University

Although direct volume rendering (DVR) has become a commodity, the design of transfer functions still a challenge. Transfer functions which map data values to optical properties (i.e., colors and opacities) highlight features of interests as well as hide unimportant regions, dramatically impacting on the quality of the visualization. Therefore, for the effective rendering of interesting features, the design of transfer functions is very important and challenging task. Furthermore, manipulation of these transfer functions is tedious and time-consuming task. In this paper, we propose a 3D spatial field for accurately identifying and visually distinguishing interesting features as well as a mechanism for data exploration using multi-

dimensional transfer function.

First, we introduce a 3D spatial field for the effective visualization of constricted tubular structures, called as a stenosis map which stores the degree of constriction at each voxel. Constrictions within tubular structures are quantified by using newly proposed measures (i.e., line similarity measure and constriction measure) based on the localized structure analysis, and classified with a proposed transfer function mapping the degree of constriction to color and opacity. We show the application results of our method to the visualization of coronary artery stenoses. We present performance evaluations using twenty-eight clinical datasets, demonstrating high accuracy and efficacy of our proposed method.

Second, we propose a new multi-dimensional transfer function which incorporates texture features calculated from statistically homogeneous regions. This approach employs parallel coordinates to provide an intuitive interface for exploring a new multi-dimensional transfer function space. Three specific ways to use a new transfer function based on parallel coordinates enables the effective exploration of large and complex datasets. We present a mechanism for data exploration with a new transfer function space, demonstrating the practical efficacy of our proposed method.

Through a study on transfer function design for DVR, we

propose two useful approaches. First method to saliently visualize the constrictions within tubular structures and interactively adjust the visual appearance of the constrictions delivers a substantial aid in radiologic practice. Furthermore, second method to classify objects with our intuitive interface utilizing parallel coordinates proves to be a powerful tool for complex data exploration.

Keywords: Direct volume rendering, transfer function, tubular structure, constriction, coronary artery stenosis, parallel coordinates
Student Number: 2011-30246

Contents

List of Tables

List of Figures

Chapter 1. Introduction

1.1 Background

1.1.1 Volume rendering

Volume rendering is a technique used to display a meaningful 2D image of a 3D volumetric dataset which is acquired by a computed tomography (CT), magnetic resonance imaging (MRI), or 3D tomosynthesis scanner. There are two fundamental types of volume rendering: surface rendering and direct volume rendering (DVR). Surface rendering converts a 3D volumetric dataset into a surface representation (i.e., polygonal meshes) which can be rendered with traditional rendering techniques. The marching cubes algorithm [1] is a common technique for extracting an isosurface which is a surface representing the locations of a constant value (i.e., isovalue) within a volume dataset. Since only surface representation is used, much of the information within data is lost. DVR visualizes 3D volumetric dataset without explicitly extracting geometric surfaces, instead uses a transfer function that maps voxel values to optical properties, such as colors and opacities [2, 3]. Among various DVR

techniques, a ray-casting DVR is usually considered to provide high image quality. The ray-casting DVR is the image-order method as its computation emanates from the output image; in contrast, the object-order method determines, for each data sample, how it affects the pixels on the output image. In the basic form, the ray-casting DVR algorithm consists of following four steps (see Figure 1.1):

- Ray casting - For each pixel of the output image, a ray is casted and traverses the volume data.
- Sampling - Along the ray lying within the volume data, the intensities are sampled at the uniform (or non-uniform [2]) intervals. Since the volume data in general is not aligned with the ray, it is necessary to interpolate the values of sample points from their surrounding voxels.

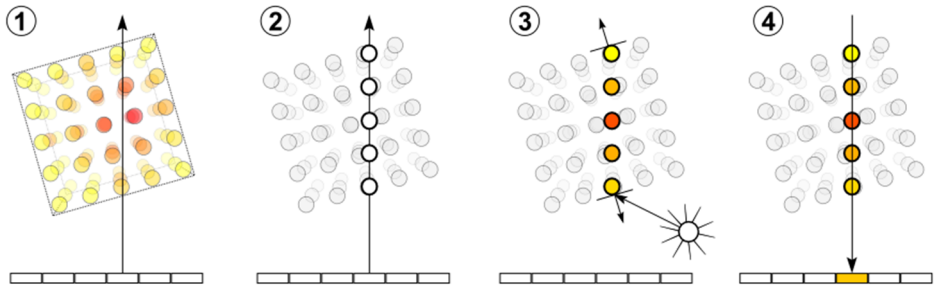

Figure 1.1 The four basic steps of the ray-casting DVR. ① Ray casting. ② Sampling. ③ Shading. ④ Compositing. Image courtesy of Wikipedia.

- Shading – The optical property of each sample point is evaluated by a transfer function, and then shaded according to its surface orientation (i.e., gradient) and the location of light.
- Compositing – The shaded sampling points are composited along the ray; the composition is derived from the rendering equation. As a result, the final color for each pixel is obtained.

One of the main challenge of DVR is the rendering of interested features with sufficient saliency so that they are visually distinguished from other structures. In DVR, transfer functions that map data values to optical properties (i.e., colors and opacities) highlight features of interests as well as hide unimportant regions, dramatically impacting on the quality of the visualization. Therefore, for the effective rendering of interesting features, the design of transfer functions is very important and challenging task.

1.1.2 Computer-aided diagnosis

Volume rendering technique is widely used in many fields of application. It has been extensively used in not only clinical applications for assisting diagnosis and operation planning but also industrial applications for non-destructive testing and reverse engineering. Among various applied fields, DVR has been most

widely used in medicine, especially in radiology. In medical applications, DVR is used for the generation of cognitive three-dimensional image from overwhelming 3D volumetric data from modern scanners (e.g., CT, MRI, and 3D tomosynthesis). Under the time pressure of clinical situation requiring prompt and important clinical decision, radiologists want 3D rendering wherein lesions of their interest are visualized distinguishably from other anatomical structures. These procedures that assist radiologists in the interpretation of medical images are called computer-aided diagnosis.

Computer-aided diagnosis, which assists radiologic interpretation by means of computer image analysis, has become one of the major research subjects in medical imaging and diagnostic radiology [3]. The basic concept of computer-aided diagnosis is to provide a second opinion in the detection and diagnostic process. The radiologists are answerable to the final interpretation of medical images. The usefulness of computer-aided diagnosis depends on the number of true-positive and false-positive markers [4]. High sensitivity (high true-positive rate) improves the performance of radiologists. For some applications, the large number of false-positive markers is not a major problem because these markers can easily be dismissed by the radiologists [5]. Nevertheless, an excessive number of false-positive markers cause the increased

reading time and detection errors. With the goals of improving accuracy in diagnosis and reducing the interpretation time, computer-aided diagnosis has been widely applied in the detection and diagnosis of many different types of abnormalities: breast cancer, lung cancer, coronary artery disease, and congenital heart defect.

1.1.3 Parallel coordinates

High-dimensional data analysis and visualization is very useful in many domains and applications [6]. Parallel coordinates [7, 8] is one of most popular and effective visualization techniques for multi-variate data in information visualization. In the parallel coordinates, each domain corresponds to a vertical axis and each data element (e.g., a N-dimensional tuple) is represented by one polyline with vertices on the parallel axes; the position of the vertex on the ith axis corresponds to the ith coordinates of the data element (see Figure 1.2). By corresponding parallel axes to dimensions, the parallel coordinates represents N-dimensional data in a 2-dimensional space.

Interaction plays an important role to enhance perception for data exploration and visual data mining [9]. The ability to interact

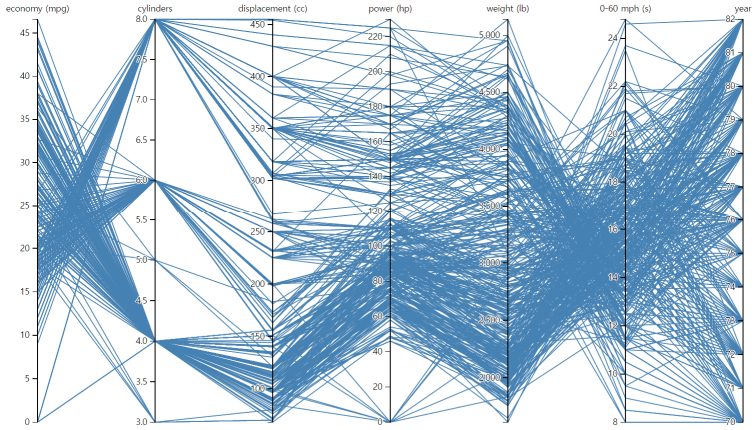

Figure 1.2 Parallel coordinates for exploring and analyzing multi-dimensional data. Each dimension corresponds to a vertical axis, and each data element is represented by one polyline crossing the parallel axes. Image courtesy of https://bl.ocks.org/jasondavies/1341281.

with visual representations (e.g., parallel coordinates) can greatly reduce the drawbacks of visualization techniques, particularly those related to visual clutter and object overlapping, providing the user with mechanisms for handling large and complex datasets [10]. The parallel coordinates allow the user to interact with the data in many ways. The user can select a subset of the data by using a brushing operation (see Figure 1.3 (a)). The selected set of the data is then used as input for subsequent operations, such as highlighting, labeling, replacing, deleting, and many more [9]. The user can also reorder parallel axes by dragging and dropping, reducing visual clutter by revealing patterns (e.g., correlations between dimensions)

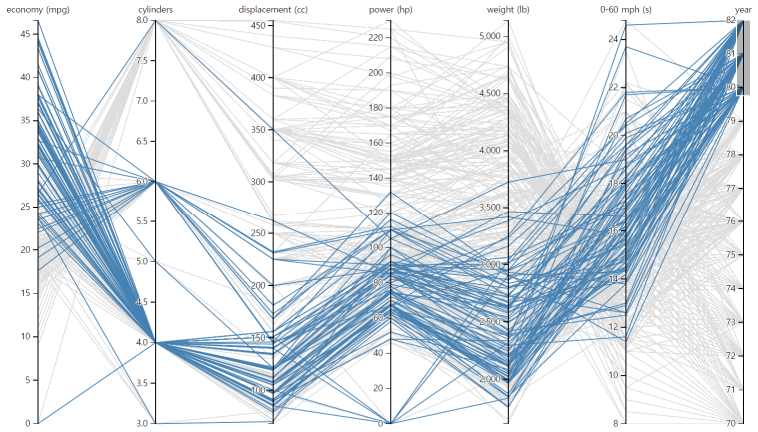

(a)

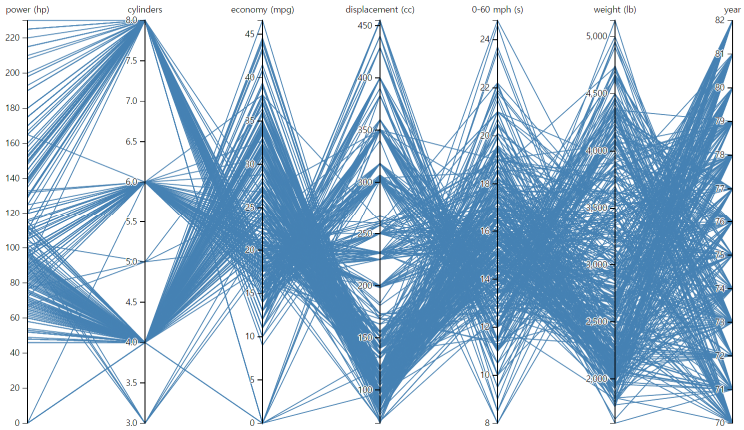

(b)

Figure 1.3 Interactions with parallel coordinates. (a) Brushing on the (right-most) year axis from 1980 to 1982. (b) Reordering. Image courtesy of https://bl.ocks.org/jasondavies/1341281.

that might have been hidden before (see Figure 1.3 (b)). These interactive parallel coordinates enable the effective exploration of large and complex datasets.

1.2 Problem statement

DVR visualizes 3D volumetric data based on transfer functions that map data values to specific optical properties (i.e., colors and opacities). These transfer functions highlight features of interest as well as hide unimportant regions, and thus, they are crucial in the exploration of 3D volumetric data. It is a challenging task to specify an appropriate transfer function which accurately identifies and visually distinguishes interesting features. In addition, manipulation of transfer functions for this classification is tedious and time-consuming task. In this paper, we deal with two main problems with transfer functions: effective rendering of interested features and efficient manipulation of transfer functions.

One of the main challenges of DVR is the rendering of interested features with sufficient saliency so that they are visually distinguished from other structures. In medicine, radiologists have used DVR for the diagnosis of lesions or diseases; they should be visualized distinguishably from other surrounding anatomical structures. Of diverse diagnostic tasks in radiology, the detection of constricted regions in complex tubular structures (e.g., coronary artery stenosis in coronary artery, intra-thoracic airway constriction, carotid artery stenosis, and intestinal obstruction) is

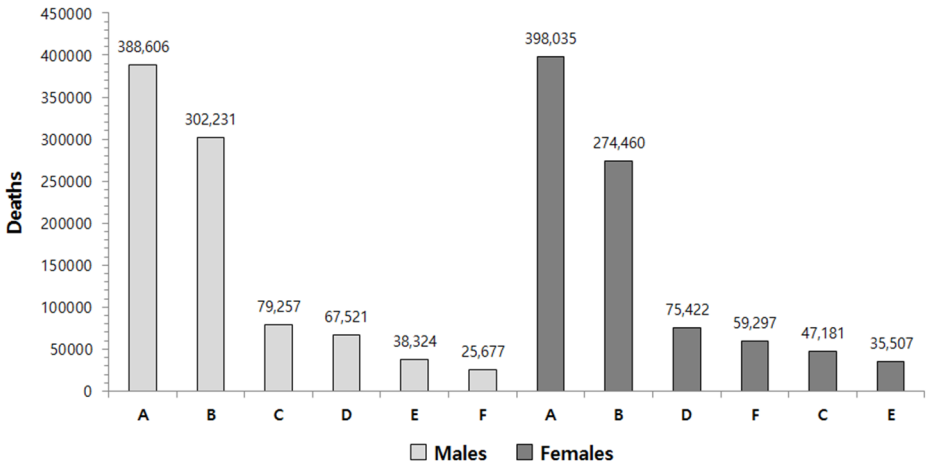

Figure 1.4 Cardiovascular disease and other major causes of death for all males and females (United States: 2011) [11]. A: Cardiovascular disease plus congenital cardiovascular disease. B: Cancer. C: Accidents. D: Chronic lower respiratory disease. E: Diabetes mellitus. F: Alzheimer disease.

one of most frequent and important diagnostic tasks. In diagnosing various diseases regarding constricted tubular structures in radiologic diagnoses, early detection of coronary artery disease (CAD) is very important because it is known to be the most common cause of death in the world [11] (see Figure 1.4).

Traditionally, invasive coronary angiography (ICA) has been considered as gold standard for assessing CAD. However, ICA is an invasive technique and did not provide the information of the plaque because it is just luminogram. Recently, coronary computed tomography angiography (CCTA) has been widely adopted to non-

invasively diagnose CAD with high diagnostic accuracy. In particular, CCTA has been reported to be useful for rapid detection of CAD in patient with acute chest pain in an emergency situation [12, 13]. However, the interpretation of CCTA requires substantial clinical expertise and experience [14]: it could take about several hours for a physician without experience of cardiac imaging to detect stenosis manually in a CCTA dataset, which may be unacceptable in the emergency situation [15]. Therefore, an imaging system that visualizes the constricted regions (i.e., stenosis) saliently can be a very helpful volume navigation tool in the CAD diagnostic procedure.

Interesting tubular structures in medicine, such as the vascular system, are typically small and tortuous and become gradually narrower as they go, covering only a few voxels in the distal part in CT or MRI images. In addition, their neighboring structures often have similar intensity with them, making it more difficult to detect (or segment) tubular structures (e.g., aorta and heart chambers neighboring coronary arteries in CCTA). Coronary artery stenoses (i.e., constrictions) within coronary arteries (i.e., tubular structures) are classified by the degree of blockage caused by coronary artery plaques including calcified, non-calcified, and mixed plaques; the degree of blockage determines the treatment for CAD including medicines, medical procedures, and surgeries. In CCTA, calcified plaques appear as small and bright regions, non-calcified plaques

have low contrast, and mixed plaques literally have mixed texture of calcified and non-calcified plaques [33]. Because of such visual difference of these three plaques, it is elusive to detect various kinds of stenoses simultaneously. Thus, the fully automated detection of such heterogeneous constrictions is a very challenging task.

Although many approaches have been proposed for effective classification, manual design of transfer functions remains a difficult and laborious task, requiring efficient manipulation mechanisms. A 1D transfer function based on scalar data values is the most commonly used one, which is difficult to differentiate the materials with similar intensities (e.g., brain and region near the skull in MRI [29]). Higher dimensional transfer functions can lead to more accurate classification since they employ more properties for each voxel, such as gradient [23, 24], curvature [25, 26], and local texture features [27]. The gradient magnitude enhances borders between different materials, and the curvature classifies specific shapes of surfaces. The local texture features identify different patterns of materials. However, as the dimension of transfer function increases, the specification of transfer function becomes more difficult. Thus, an intuitive and efficient user interface for specifying these higher dimensional transfer functions is crucial to explore and understand a volume dataset with DVR.

1.3 Main contribution

In this study, we propose a 3D spatial field for effective classification of constricted tubular structures, called as stenosis map. For ease of explanation, we describe the proposed approach with an exemplary application to coronary artery stenoses; but, this approach can be directly applied to other constricted tubular structures only with relevant parameter exploration. Furthermore, we present a mechanism for data exploration based on parallel coordinates for multi-dimensional transfer function design.

The proposed method for effective volume visualization of constricted tubular structures consists of the following three main steps, as shown in Figure 1.5. First, we detect tubular structures by using a newly proposed similarity measure to line (i.e., line similarity), which serve as the search space of the subsequent stenosis map computation. This search space restriction reduces false positive and improves accuracy in the constriction detection step. The newly proposed similarity measure to line is derived from the localized structure analysis based on the Hessian matrix, which is calculated after applying Gaussian prefiltering; the optimal Gaussian scale selection is important in the Gaussian prefiltering. In this study, we use the mean diameter of the coronary artery which

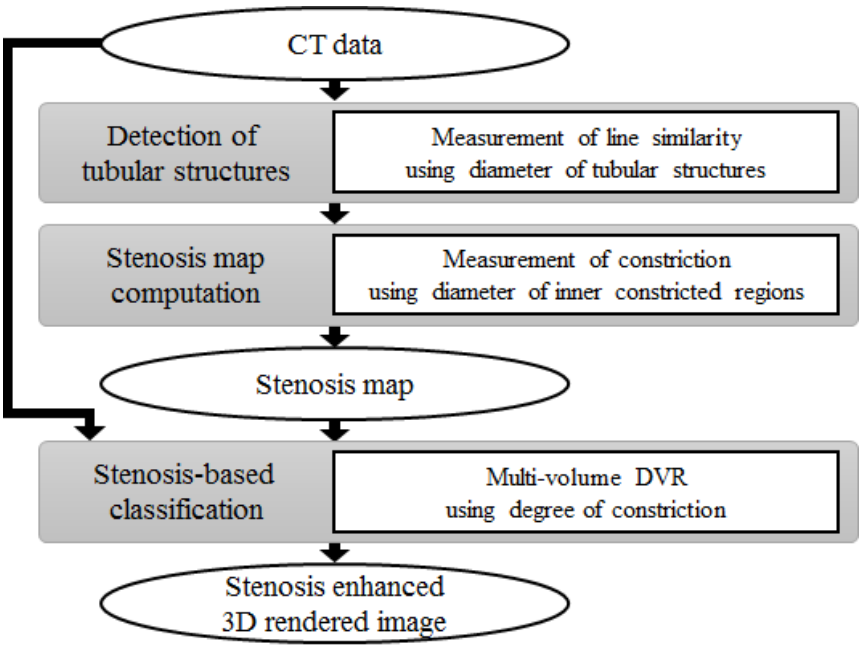

Figure 1.5 Process of effective volume visualization of constricted tubular structures.

is calculated from the coronary angiography procedure. For the application to other tubular structures, the diameter for the given tubular structures can be used.

And then we quantify constrictions within the previously detected tubular structures by using a newly proposed constriction measure which is also derived from the Hessian matrix. In a similar manner as in the selection of optimal Gaussian scale for the coronary artery, we determine the optimal Gaussian scale for the stenosis using the degree of stenosis severity which is assessed by the percentage of obstruction in the lumen diameter. For the

application to other kinds of constrictions, relevant constriction threshold (e.g., 50% obstruction in CCTA) can be used. As a result of quantifying constrictions within tubular structures, we obtain a 3D spatial field of stenosis map, of which each voxel has a scalar value of its corresponding degree of constriction.

Finally, the stenosis map is rendered simultaneously with the input volume data by using multi-volume DVR. While a ray traverses both volume datasets simultaneously, it samples the intensity from the input volume data and the degree of constriction from the stenosis map at a uniform interval. And it accumulates the color and opacity that can be evaluated using a newly proposed transfer function. Also, we propose a new opacity modulation technique (i.e., constriction-magnitude-based opacity modulation), which delivers a clear visualization of the inner stenoses. Such stenosis-based classification enables easy and intuitive adjustment of the visual appearance of constrictions within tubular structures. The performance evaluation using twenty-eight clinical datasets shows that constricted regions are accurately encoded into the stenosis map and saliently visualized, demonstrating that our method can be an effective volume exploration tool in various, including but not limited to medicine, application fields of DVR.

We also propose a data exploration method based on parallel coordinates. Our data exploration method uses the statistical and

texture features to define a new multi-dimensional transfer function which is able to achieve the desired classification of objects in DVR. First, we extract the statistical features (i.e., mean value and standard deviation) using adaptive growing technique which also extrudes the relative size of the local feature at each voxel. Second, we calculate the texture features (i.e., entropy and homogeneity) using adaptive block based gray-level co-occurrence matrix (GLCM) which is defined based on the previously computed relative size at each voxel. Finally, we define a new multi-dimensional transfer function incorporating previously computed statistical and texture features, which employs parallel coordinates wherein each voxel is represented as a polyline with parallel axes of individual multi-dimensional features. Multi-dimensional transfer function design with parallel coordinates enables more interactive exploration of the transfer function space with multi-variate features. The step-by-step illustration of our data exploration method shows that the parallel coordinate representation can be used as a tool to help users in specifying a transfer function to classify or segment a large and complex dataset.

1.4 Organization of dissertation

The remainder of this paper is organized as follows. The next chapter briefly review previous researches in the transfer functions of DVR, segmentation of coronary artery stenosis and parallel coordinates. Chapter 3 introduces an effective volume visualization technique for constricted tubular structures. For ease of explanation, we describe the proposed approach with an exemplary application to coronary artery stenoses; but, this approach can be directly applied to other constricted tubular structures only with relevant parameter exploration. Chapter 4 presents a data exploration method based on parallel coordinates, followed by conclusion in Chapter 5.

Chapter 2. Related Work

2.1 Transfer function

DVR visualizes 3D volumetric data without explicitly creating intermediate geometric structures (i.e., meshes composing an isosurface); instead, transfer functions make volumetric data visible by mapping data values to optical properties (i.e., colors and opacities). Transfer functions highlight features of interest as well as hide unimportant regions, dramatically affecting the quality of the visualization. Although DVR has become a commodity, the design of transfer function is still a challenge.

2.1.1 Transfer functions based on spatial characteristics

One of the main challenges of DVR is the specification of an appropriate transfer function that accurately identifies and visually distinguishes interesting features. For these accurate classification, some approaches used spatial characteristics derived by analyzing around a voxel instead of voxel's properties (e.g., intensity,

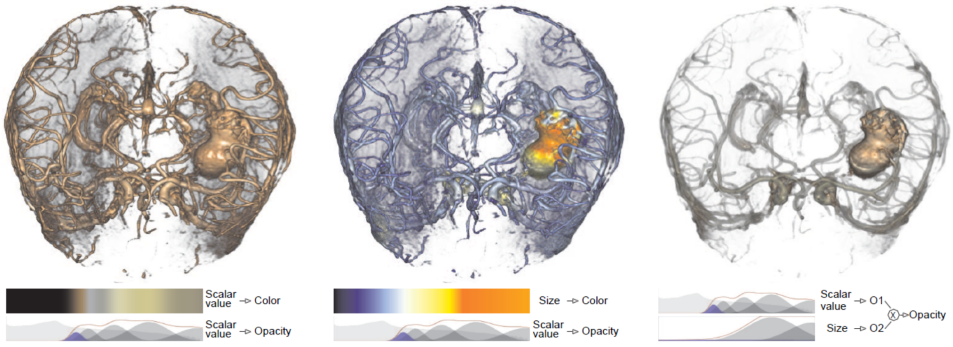

Figure 2.1 Size-based classification of an aneurysm. Left: 1D transfer function based on scalar value. Middle: Size-based classification, where size maps to color and scalar value to opacity. Right: Size-based classification, where opacity is the product of opacity mappings from both scalar value and size. Color mapping is same as left. Image courtesy of Correa and Ma [16].

gradient, and curvature). Correa and Ma [16] proposed size-based transfer functions that mapped the relative size of features to color and opacity. Size-based transfer functions were achieved with the use of scale fields, which are scalar fields where every voxel represents the local scale or size of the feature containing that voxel. These scale-fields were computed via scale-space analysis and a set of detection filters. Unlike other complex spaces, size can be defined in a single dimension and it complements easily traditional transfer functions (see Figure 2.1). They also proposed a 2D transfer function based on occlusion spectrum which is distribution of ambient occlusion that can be interpreted as a

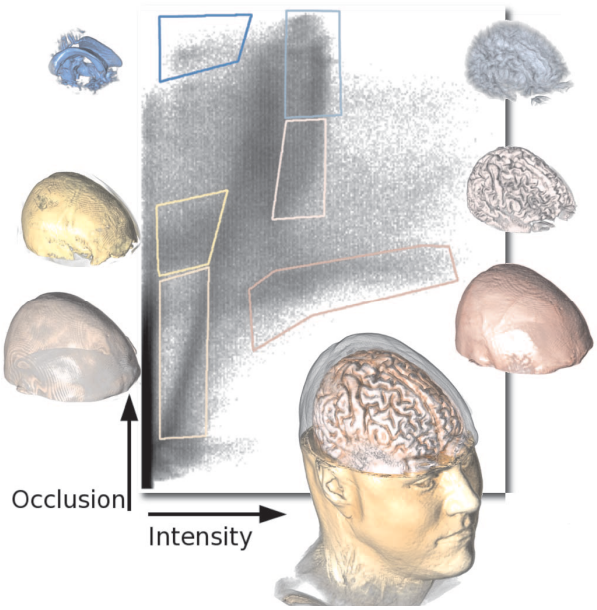

Figure 2.2 Occlusion spectrum for an MRI dataset. Anatomical structures (e.g., skull, brain, and ventricles) appear depending on how internal they are. Image courtesy of Correa and Ma [17].

weighted average of the intensities in a spherical neighborhood around each voxel [17]. Occlusion spectrum encodes the contribution of the voxels in the neighborhood of a given point, and exhibits spatial coherence, important for identifying features and their spatial relationships. When combined with the intensity values, the occlusion spectrum provides a classification space that separates features that are highly occluded (e.g., separation of interior objects from outer objects) (see Figure 2.2). Also, many other approaches relying on local neighborhood analysis have been proposed, including statistical transfer function space [18] and

shape-based classification [19-21].

In this paper, we propose a new spatial field that can deliver a new dimension for salient visualization of constrictions within tubular structures, called as a stenosis map. The stenosis map is derived by analyzing local structural features around a voxel, and used to design a new transfer function which maps the degree of constriction to color an opacity, complementing easily traditional transfer function unlike other complex spaces.

2.1.2 Opacity modulation techniques

In order to enhance important features or suppress unwanted details, opacity modulation techniques have been proposed. A common method is gradient-magnitude opacity modulation. Levoy [23] modulated the opacity according to the magnitude of the local gradient, enhancing boundaries and suppressing homogeneous regions. Bruckner *et al.* [22] introduced context-preserving volume rendering technique which modulated the opacity of a sample in order to simultaneously visualize interior and exterior structures while retaining context information. The opacity of a sample is modulated by a function of shading intensity, gradient magnitude, distance to the eye point, and previously accumulated opacity to

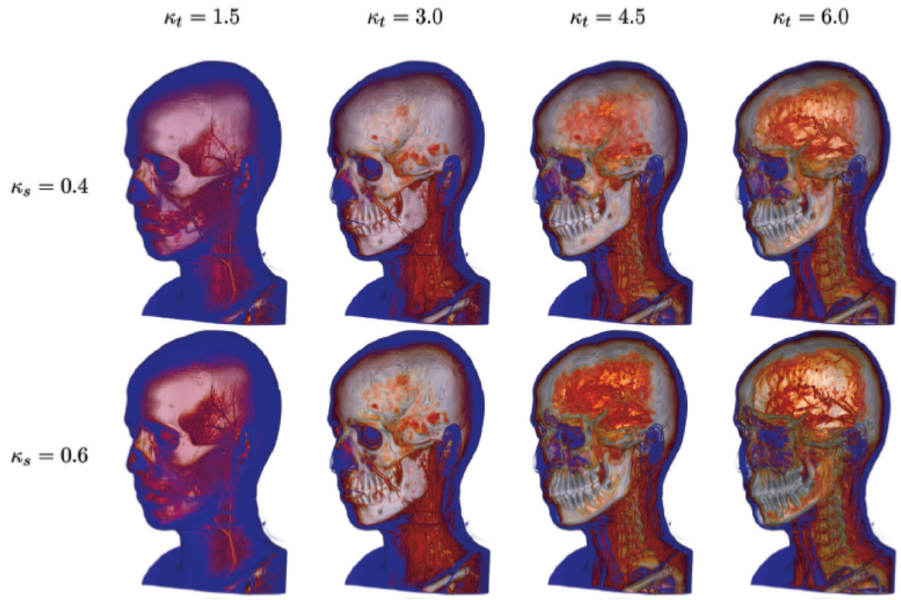

Figure 2.3 Context-preserving volume rendering of a contrast-enhanced CT angiography dataset using different values of the two parameters. Columns have the same κ_t value and rows have the same κ_s value. Image courtesy of Bruckner *et al.* [22].

selectively reduce the opacity in less important data regions. By means of the two user-specified parameters, the user can interactively uncover occluded regions (see Figure 2.3). These opacity modulation techniques are applicable to any type of transfer functions without restrictions.

In this paper, we propose a new opacity modulation technique (i.e., constriction-magnitude-based opacity modulation), which delivers a clear visualization of the inner stenoses. When rendering the contrasted tubular structures (i.e., contrasted coronary arteries

in CCTA), they are displayed with high opacity, often blocking the constrictions inside them. To resolve this problem, we introduce an opacity modulation technique.

2.1.3 Multi-dimensional transfer functions

A 1D transfer function based on scalar data values is the most commonly used one, which is difficult to differentiate the materials with similar intensities (e.g., brain and region near the skull in MRI [29]). Higher dimensional transfer functions can lead to more accurate classification since they employ more properties for each voxel, such as gradient [23, 24], curvature [25, 26], and local texture features [27]. Kindlmann *et al.* [26] advances the use of curvature information in multi-dimensional transfer functions, with a methodology for computing high-quality curvature measurements. Curvature-based transfer functions extend the expressivity and utility of DVR through contributions in three different applications: non-photorealistic volume rendering, surface smoothing via anisotropic diffusion, and visualization of isosurface uncertainty (see Figure 2.4). Caban and Rheingans [27] used textural properties to differentiate materials. For each subvolume of interest, multi-dimensional texture-based descriptor is computed, which

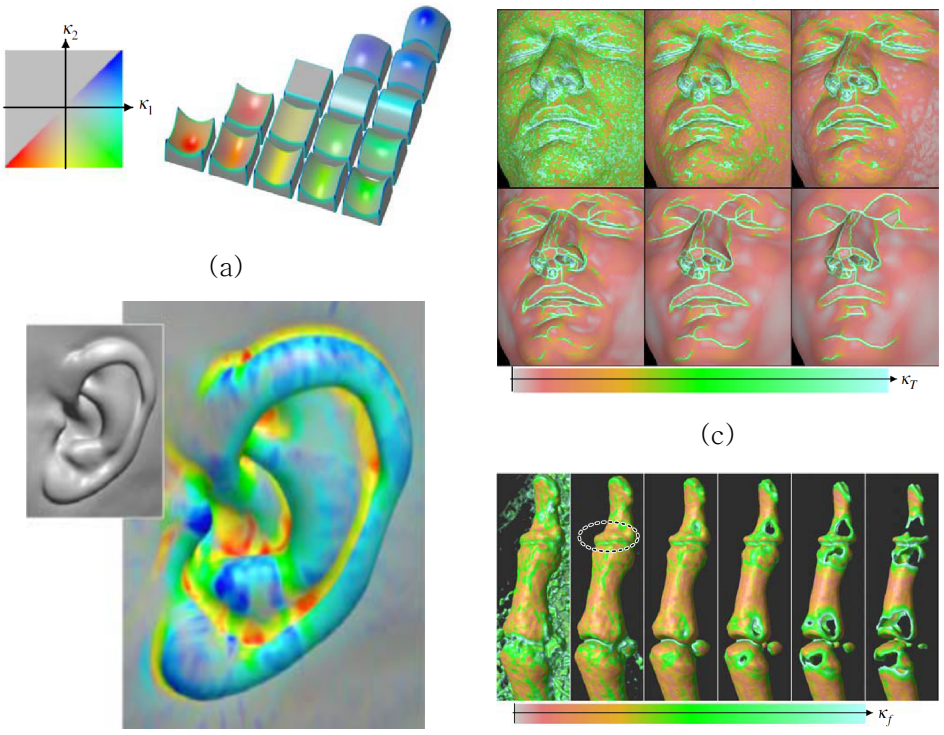

(a) (c)

(b) (d)

Figure 2.4 Applications of curvature-based transfer functions. (a) Volume rendered diagram of (κ_1, κ_2) space. (b) Non-photorealistic volume rendering using transfer function from (a). (c) Surface smoothing via anisotropic diffusion. (d) Visualization of isosurface uncertainty. Image courtesy of Kindlmann *et al.* [26].

captures the local textural statistical properties: first- (e.g., skewness and kurtosis), second- (e.g., energy and entropy), and high-order statistics (e.g., short run and long run). All the statistical descriptors are pre-computed and stored in a vector image, which is used to look up the voxel's properties during the

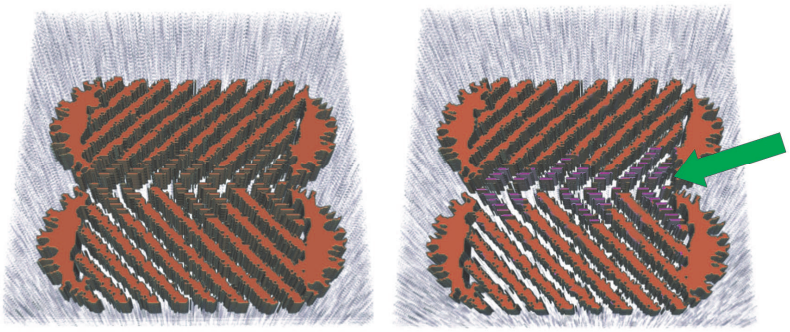

Figure 2.5 Texture-based classification. Left: Synthetic data being visualized with the standard transfer function. Right: The same dataset visualized using texture-based transfer function. The center of the volume (pointed by the arrow) can be highlighted by analyzing local textural properties. Image courtesy of Caban and Rheingans [27].

ray-casting DVR. Structures and features with the same intensity can be visualized with different rendering properties (see Figure 2.5).

In this paper, we propose a new multi-dimensional transfer function space using the statistical and texture features (i.e., mean value, standard deviation, relative size, and texture features). This approach successfully discriminates different objects with the similar intensities using our intuitive interface utilizing parallel coordinates.

2.1.4 Manipulation mechanism for transfer functions

Although many approaches have been proposed for effective classification, manual design of transfer functions remains a difficult and laborious task, requiring efficient manipulation mechanisms. In order to simplify the user interaction with the transfer function, Kniss *et al.* [28] introduced the concept of dual domain (spatial domain and transfer function domain) interaction (see Figure 2.6).

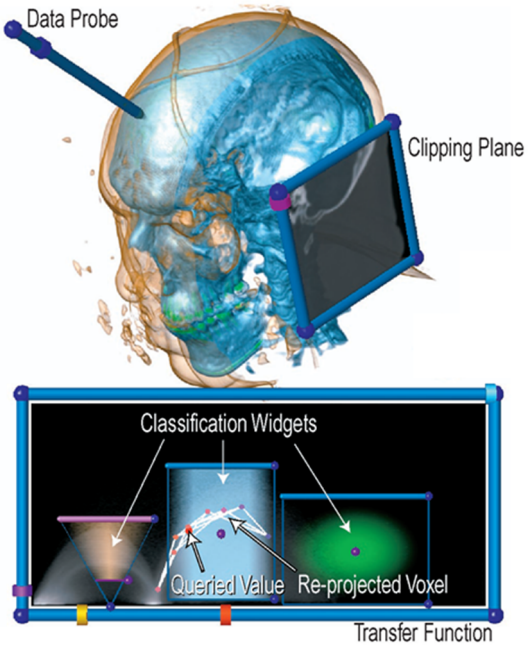

Figure 2.6 Dual domain interaction. Top: Spatial domain. The user points at the feature of interest using a data probe or a clipping plane. Bottom: Transfer function domain. The user assigns the visual attributes to the reprojected values. Image courtesy of Kniss *et al.* [28].

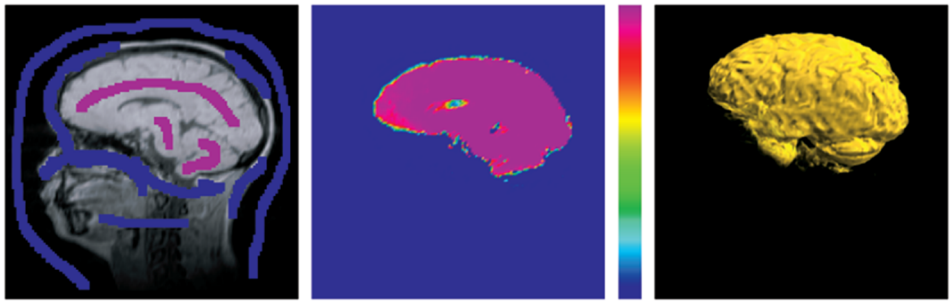

Figure 2.7 Painting user interface. Left: A slice painted by a user (pink: features of interest, blue: undesirable materials). Middle: The result of classification with a color bar. Right: The rendered result of the classified volume. Image courtesy of Tzeng *et al.* [29].

In the spatial domain, the user points at a location of interest using a data probe or a clipping plane. The values at that point are visualized in the transfer function domain, and the user can then begin specifying a custom transfer function. With this approach, the conceptual gap between domains is significantly lessened, effectively simplifying the complicated task of specifying a multi-dimensional transfer function. Tzeng *et al.* [29] provides a painting user interface that is used to automatically define high-dimensional classification functions (see Figure 2.7). The user specifies regions of interest by simply painting on a few slices from the volume data. The painted voxels are used in an iterative training process, and then the entire volume data can be classified. Such a system employing a machine learning method using the painted regions as

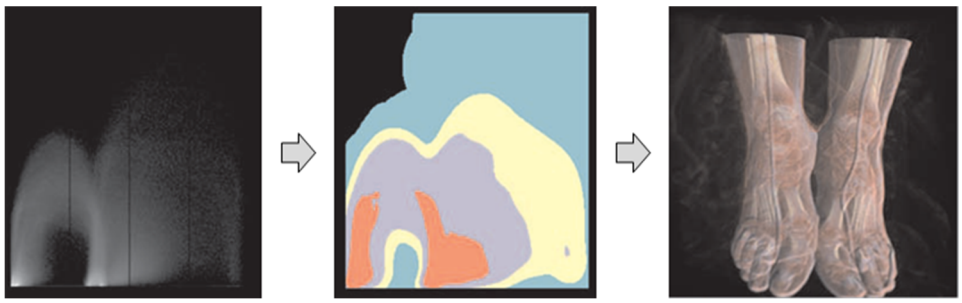

Figure 2.8 Non-parametric clustering within the transfer function space. Left: Value versus value gradient histogram. Middle: The generated transfer function using non-parametric clustering. Right: The rendered result. Image courtesy of Maciejewski *et al.* [31].

training data enables the user to perform classification in a much higher dimensional space without explicitly specifying the mapping for every dimension used. Roettger *et al.* [30] presented a method that groups spatially connected regions in the 2D histogram used for classification. In the transfer function domain, each feature (connected regions in the spatial domain) is segmented by using the voxel barycenter and the region variance, assisting manual specification of colors for similar features. Likewise, Maciejewski *et al.* [31] applied a non-parametric clustering within the transfer function domain in order to extract patterns and guide transfer function generation (see Figure 2.8).

In this paper, we propose a data exploration method based on parallel coordinates for multi-dimensional transfer function design.

Our intuitive interface utilizing parallel coordinates enables more interactive exploration of the transfer function space with multi-variate features, crucial to understand large and complex datasets.

2.2 Coronary artery stenosis

CAD is the most common type of heart disease, leading cause of death in the world [11]. It occurs when coronary arteries, which supply blood (including oxygen and nutrients) to the myocardium, become narrow or occluded due to the build-up of plaques (e.g., calcium, fat, and cholesterol). These narrowing of a vessel is referred to as stenosis, leading complications such as chest pain or heart attack. In order to determine the appropriate clinical procedure of patients with acute chest pain, it is crucial to diagnose the presence and severity of coronary artery stenosis. CCTA is a non-invasive evaluation procedure for the diagnosis of CAD with high diagnostic accuracy, allowing the interpreter to assess the presence, extent, and type of coronary artery plaques [41]. Several studies have shown that CCTA is very useful to detect CAD rapidly for a patent who complained acute chest pain in the emergency situation [12, 13]. However, the interpretation of CCTA requires substantial clinical expertise and experience [14]: it could take

about several hours for a physician without experience of cardiac imaging to detect stenosis manually in a CCTA dataset, which may be unacceptable in the emergency situation [15]. Therefore, an automated system that can identify the stenosis fast and accurately could be an assistant or alternative to the physicians in an emergency.

There have been many approaches in the image segmentation field that tried to detect coronary artery stenosis automatically or semi-automatically. They can be categorized into two groups: segmentation- and feature-based methods.

Segmentation-based methods detect stenoses by estimating a vessel diameter after lumen segmentation. Some methods incorporated both a new lumen segmentation algorithm and a new stenosis detection algorithm. On the other hand, other methods employed a previously published lumen segmentation algorithm, and then proposed a new stenosis detection algorithm (refer interested readers to [32] for complete survey of lumen segmentation). Wesarg *et al.* [33] proposed a tracking-based segmentation which progresses along the vessel by iterative prediction and correction steps. The predicted centerline is corrected by the center of cross-sectional contour points. And the stenosis is then detected by using the diameter information and intensity analysis. This method only detected calcified plaques and required substantial

user involvement. Saur *et al.* [34] employed a rule-based technique which involved the extraction and registration of lesion candidates in both contrast-enhanced and non-contrast-enhanced CT images. The prior-segmentation of coronary artery is used to restrict the lesion candidates to only those within the coronary arteries. This method automatically detected calcified plaques using distance (between corresponding plaques of two images) and intensity score rules. Although the registration step significantly reduced the false positive rate, it made patients exposed to unnecessary radiation with those two CT image acquisitions. Xu *et al.* [35] proposed a fuzzy segmentation method in which each voxel has the probability to belong to a target object. The segmentation of coronary artery is accomplished using a previously published method by Yang *et al.* [36] which is a hybrid strategy using multi-scale filtering and a Bayesian probabilistic approach within the level set segmentation model. In following, for measuring local diameters along a coronary artery centerline, they adopted the fuzzy distance transform which is the smallest fuzzy distance from the boundary, and used these distance values for detecting and quantifying stenoses. These segmentation-based methods are highly dependent on the result of lumen segmentation which usually requires a lot of manual interactions.

Feature-based methods, which use machine learning

techniques to reduce manual interactions, detect stenoses using features computed along the centerline of a vessel. Mittal *et al.* [37] designed a cylindrical sampling pattern with the axis of cylinder aligned to the centerline of coronary artery. Since stenoses can occur anywhere around the axis, they used features which are rotation invariant about the axis to detect calcified plaques. Teßmann *et al.* [38] also employed a cylindrical pattern and used intensity variance, entropy, and Harr-like features to detect both calcified and non-calcified plaques. These feature-based methods used supervised schemes so that it is laborious to collect manually labeled data for all types of lesions. Zuluaga *et al.* [39] attempted to use an unsupervised scheme which does not require any labeled data for training. However, bifurcations were falsely detected as stenoses in this method. To overcome this shortcoming, they proposed a semi-supervised scheme in [40]. In this method, the training set is made of both unlabeled data and a small amount of data labeled as normal.

Unlike these previous methods that usually require a lot of manual interactions [33-35], or laborious manual data classification [37, 38, 40], we analyze the localized structure for the efficient and accurate detection of coronary arteries and inner stenoses. We compared the result of our method with those of 11 recently

proposed methods, which were presented at MICCAI 2012 workshop, '3D Cardiovascular Imaging: a MICCAI segmentation challenge' [41]. This challenge was aimed at quantitatively evaluating the algorithms for coronary artery stenoses detection/ quantification and lumen segmentation in CCTA, and conducted using a database that consists of multi-center multi-vendor CCTA datasets. Using the database for this challenge, we measured and compared the detection accuracy results.

2.3 Parallel coordinates

Parallel coordinates [7, 8], which is one of most popular and effective visualization techniques for multi-variate data in information visualization, has been used for specifying and visualizing higher dimensional classifier in DVR [42-45]. Lum *et al.* [44] developed a user interface for effectively exploring and utilizing the multi-scale volume data generated by the filter bank to refine volume classification. As illustrated in Figure 2.9, the top row (Level 0) represents the distribution of data values for the original, unfiltered volume. The lines moving downward through the subsequent levels represent data values' response to progressively

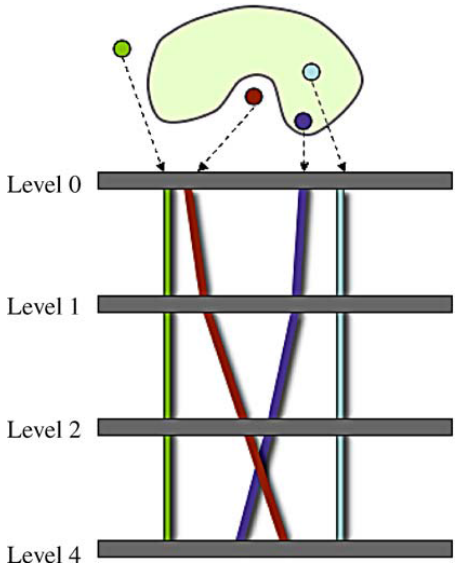

Figure 2.9 User interface for utilizing the multi-scale volume data generated by the filter bank to refine volume classification. The thick horizontal lines are coordinate axes corresponding to a particular filtered data level. Each colored line corresponds to the data value of a sample point in each filter level. Image courtesy of Lum *et al.* [44].

stronger filtering. User interaction starts with specifying a 1D transfer function for the top, and then this transfer function is refined by inserting additional classification widgets, as necessary, at varying filter levels (see Figure 2.10). Zhao and Kaufman [45] also utilized parallel coordinates for the design of the transfer function. For each voxel of input dataset, various high dimensional parameters (i.e., sixteen statistical attributes such as contrast, correlation, and angular second moment) are calculated. And then, parameters are selected according to the patterns of corresponding

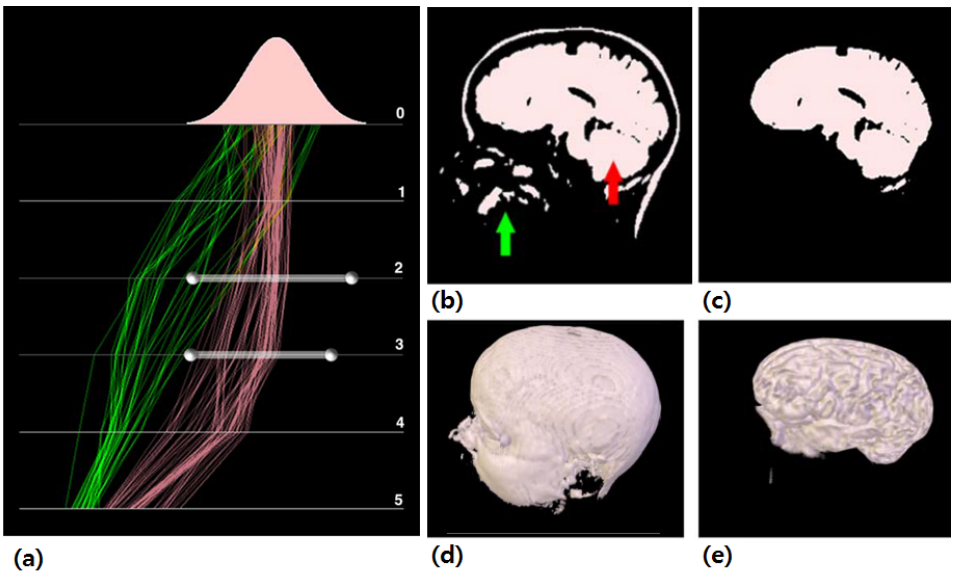

Figure 2.10 Refinement of the transfer function. The bundles of pink and green lines in (a) are the result of user probes of the wanted (red) and unwanted (green) areas in (b). The mixing of values at level zero indicates overlapping intensity values. However, the clear separation into pink and green bundles at subsequent filter levels suggest that a higher dimensional classification can help. (b) and (d) show the result of applying the defined transfer function at level zero. Adding a classification widget at level two and three produced the improved results shown in (c) and (e). Image courtesy of Lum *et al.* [44].

polylines drawn in parallel coordinates. For the high dimensional transfer function design, the user can choose to either interactively design special widgets on the coordinates directly or automatically project all the attribute parameters to the 2D space by the local linear embedding technique as dimension reduction, and then assign

colors and opacities to the classes calculated by a k-mean algorithm in the 2D space.

In this paper, we propose a data exploration method based on parallel coordinates. Our data exploration method uses the statistical and texture features to define a new multi-dimensional transfer function. Adaptive growing technique is used to extract the statistical features (i.e., mean value and standard deviation), which keeps the neighborhood within the same material and enhances the accuracy of the subsequent texture analysis step. The relative size of the local feature at each voxel, which is also extruded by adaptive growing technique, is used to calculate the texture features (i.e., entropy and homogeneity) based on GLCM. Using calculated statistical and texture features, we define a new multi-dimensional transfer function using parallel coordinates. The step-by-step illustration of our data exploration method shows that the parallel coordinate representation can be used as a tool to help users in specifying a transfer function to classify or segment a complex dataset.

Chapter 3. Volume Visualization of Constricted Tubular Structures

3.1 Overview

First, we propose a 3D spatial field for the effective visualization of constricted tubular structures, called as a stenosis map which stores the degree of constriction at each voxel. Constrictions within tubular structures are quantified by using newly proposed measures (i.e., line similarity measure and constriction measure) based on the localized structure analysis, and classified with a proposed transfer function mapping the degree of constriction to color and opacity. We show the application results of our method to the visualization of coronary artery stenoses. We present performance evaluations using twenty-eight clinical datasets, demonstrating high accuracy and efficacy of our proposed method. The ability of our method to saliently visualize the constrictions within tubular structures and interactively adjust the visual appearance of the constrictions proves to deliver a substantial aid in radiologic practice.

3.2 Localized structure analysis

To classify the constrictions within tubular structures, we use local structural features in this paper. Let $I(\mathrm{x})$ denote the density value at a point $\mathrm{x} = (x_0, x_1, x_2)$ in input volume data. The local structure of $I(\mathrm{x})$ in a neighborhood of x can be approximated by the Taylor expansion [46].

$$I(\mathrm{x}+\Delta\mathrm{x}) = I(\mathrm{x}) + \Delta\mathrm{x}^T \nabla I(\mathrm{x}) + \frac{1}{2}\Delta\mathrm{x}^T H(\mathrm{x})\Delta\mathrm{x} \ , \tag{3.1}$$

where ∇I is the gradient vector and $H(\mathrm{x})$ denotes the Hessian matrix, which is a matrix built of the second partial derivatives of $I(\mathrm{x})$ as follows:

$$H(\mathrm{x}) = \begin{bmatrix} \frac{\partial^2 I}{\partial x^2} & \frac{\partial^2 I}{\partial x \partial y} & \frac{\partial^2 I}{\partial x \partial z} \\ \frac{\partial^2 I}{\partial y \partial x} & \frac{\partial^2 I}{\partial y^2} & \frac{\partial^2 I}{\partial y \partial z} \\ \frac{\partial^2 I}{\partial z \partial x} & \frac{\partial^2 I}{\partial z \partial y} & \frac{\partial^2 I}{\partial z^2} \end{bmatrix} . \tag{3.2}$$

At each voxel position x, we calculate the second derivatives and construct the Hessian matrix. By the eigenvalue decomposition of the Hessian matrix, we obtain three eigenvalues, λ_1, λ_2, and λ_3

Table 3.1 Basic conditions for each localized structure [47]

Localized structure	Eigenvalue signature
Sheet (e.g., cortex)	$\lambda_3 \ll \lambda_2 \simeq \lambda_1 \simeq 0$
Line (e.g., vessel, bronchus)	$\lambda_3 \simeq \lambda_2 \ll \lambda_1 \simeq 0$
Blob (e.g., nodule)	$\lambda_3 \simeq \lambda_2 \simeq \lambda_1 \ll 0$

($\lambda_1 \geq \lambda_2 \geq \lambda_3$) and their corresponding eigenvectors, e_1, e_2, and e_3. The combination of these three eigenvalues, called as eigenvalue signature, characterizes the local morphologic structure of an object. Sheet, line, and blob structures can be classified using the conditions summarized in Table 3.1, assuming that bright structures exist in a dark background [47]. Measurements of similarity to a specific localized structure can be derived from these basic conditions. Specially, this localized structure analysis has been successfully applied to detect tubular structures (e.g., vascular trees [48–50], or airway trees [51]).

In practice, the second derivatives are calculated after applying the Gaussian filter to input volume data. The Gaussian filter is specified by its standard deviation, called as Gaussian scale, and the Gaussian scale can be fixed for the detection of single-scale objects or ranged for the detection of multiple-scale objects. For the accurate localized structure analysis based on the Hessian

matrix, it is important to use an optimal Gaussian scale at the stage of Gaussian prefiltering. The optimal value of Gaussian scale for a target object with a diameter d is proven to be $d/4$ [52]. Using the optimal Gaussian scale, the proposed method performs two steps of localized structure analysis targeting two different objects of a tubular structure and inner constrictions. Each analysis uses the optimal Gaussian scale corresponding to its target object.

3.3 Stenosis map

3.3.1 Overview

The first step of classifying constricted tubular structures is the estimation of input volume data to encode the degree of constriction, resulting in the stenosis map. In order to discriminatingly visualize coronary artery stenoses caused by all types of plaques, we compute the stenosis map by analyzing the localized structure around a voxel; we propose measurements of similarity to a specific localized structure. In the stenosis map, each voxel has a scalar value of its corresponding degree of constriction, understood as how constricted it is relative to surrounding tubular structures. The

process of computing the stenosis map consists of the following two procedures. Fist, tubular structures are detected by using a newly proposed similarity measure to line (i.e., line similarity), which serves as the search space of the subsequent stenosis map computation. Second, from the previously detected tubular structures, inner constricted regions are detected by using a newly proposed constriction measure; and their degree of constriction are calculated, resulting in the stenosis map.

3.3.2 Detection of tubular structures

Interesting tubular structures in medicine, such as the vascular system, are typically small and tortuous and become gradually narrower as they go, covering only a few voxels in the distal part in CT or MR images. In addition, their neighboring structures often have similar intensity with them, making it more difficult to detect (or segment) tubular structures (e.g., aorta and heart chambers neighboring coronary arteries in CCTA).

Now, we elaborate on the computation of the stenosis map with exemplary application to coronary artery stenosis; however, its application to other tubular structures is straightforward with easy-to-follow parameter exploration (detailed in Section 3.6.5).

Coronary artery stenoses (i.e., constrictions) within coronary arteries (i.e., tubular structures) are classified by the degree of blockage caused by coronary artery plaques including calcified, non-calcified, and mixed plaques. In CCTA, calcified plaques appear as small and bright regions, non-calcified plaques have low contrast, and mixed plaques literally have mixed texture of calcified and non-calcified plaques [33]. Because of such visual difference of these three plaques, it is elusive to detect various kinds of stenoses simultaneously. Such heterogeneous constrictions are not rare in medicine, making the radiologic diagnosis more difficult.

Prior to detection coronary artery stenoses, we first find tubular structure of coronary arteries to restrict the search space of the subsequent constriction detection step. This search space restriction reduces false positive and improves accuracy in the constriction detection step. The tubular structures of coronary arteries are detected by using a newly proposed similarity measure derived from the Hessian matrix.

As discussed before, the optimal Gaussian scale selection in the Gaussian prefiltering is important in the localized structure analysis based on the Hessian matrix. In this study, we use the mean diameter of the coronary artery when determining the optimal Gaussian scale for the coronary artery detection. The mean diameter of the coronary artery is calculated from the coronary

Table 3.2 Diameters of coronary artery [53]

Vessel type	QCA diameters	
	Mean ± SD	Range
LM	5.07 ± 0.75	3.82 – 6.09
LAD	3.30 ± 0.85	1.46 – 5.28
LCX	3.53 ± 0.76	1.52 – 5.27
RCA	3.61 ± 0.58	2.71 – 5.67
Total	3.57 ± 0.84	1.46 – 6.09

Note. Data are in millimeters. LM = left main. LAD = left anterior descending branch. LCX = left circumflex branch. RCA = right coronary artery.

angiography procedure that quantitatively measures coronary artery dimensions [53] (see Table 3.2). The severity of stenosis is assessed by the percentage of obstruction in the lumen diameter; a normal vessel is 0% stenosis. To differentiate the coronary artery stenosis with ≥ 20% obstruction in CCTA, the isotropic spatial resolution of CT should be at least 0.3 mm [54]. Considering the anatomical information about the coronary artery [53, 54], the diameter of a coronary artery is about 9−15 voxels in coronary CT data with a spatial resolution of 0.3 mm. Therefore, the optimal Gaussian scale for the coronary artery is set to be less than 3.75 (=15/4). For the application to other tubular structure, the diameter

for the given tubular structures can be used.

After the Gaussian prefiltering, the tubular structures of coronary arteries are detected by a proposed similarity measure to line. At each voxel position, we calculate a similarity measure to line SM_{line}, called as line similarity, given by:

$$SM_{line} = \begin{cases} 1 & if \quad \lambda_3 \le \lambda_2 \le \lambda_1 < 0 \quad and \\ & \quad R_{blob} < T_{blob} \quad and \\ & \quad R_{sheet} > T_{sheet} \quad and \\ & \quad R_{noise} > T_{noise} \quad and \\ & \quad G_{\lambda_1} < T_G \\ 0 & otherwise \end{cases}, \tag{3.3}$$

where

$$R_{blob} = \frac{|\lambda_1|}{\sqrt{|\lambda_2 \lambda_3|}}, \tag{3.4}$$

$$R_{sheet} = \frac{|\lambda_2|}{|\lambda_3|}, \tag{3.5}$$

$$R_{noise} = \sqrt{{\lambda_1}^2 + {\lambda_2}^2 + {\lambda_3}^2}. \tag{3.6}$$

The line similarity involves three measures, R_{blob}, R_{sheet}, and R_{noise} of Frangi *et al.* [55]. R_{blob} detects blob-like structure: it reaches its maximum value for a blob-like structure and is close to zero for line-like structure ($\lambda_1 \approx 0$) or sheet-like structure ($\lambda_2 \approx \lambda_1 \approx 0$).

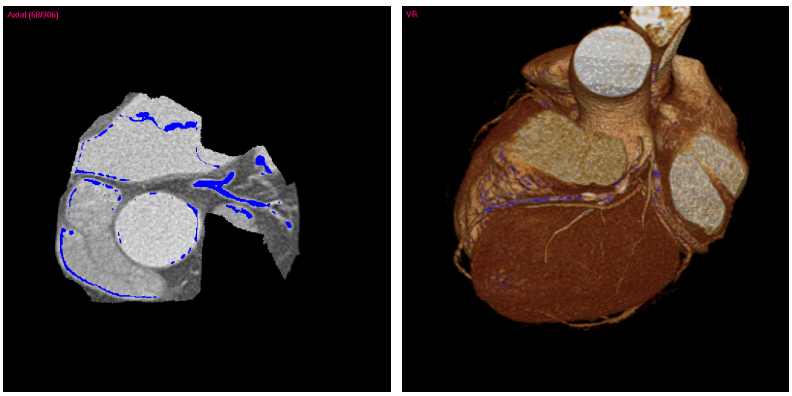

(a) (b)

Figure 3.1 Coronary artery detection of (a) a 2D slice image and (b) a 3D rendered image of CCTA. The detected coronary artery is used to restrict the search space of the subsequent constriction detection step, reducing false positive and improving accuracy.

R_{sheet} distinguishes between line- and sheet-like structures: when $|\lambda_3| \gg |\lambda_2| \approx 0$ (R_{sheet} being smaller), the structure is more likely to be sheet-like rather than line-like. R_{noise} minimizes the influence of image noise: it gets small in the background where there is no structure; and it gets great in high-contrast regions when at least one of the eigenvalues is large. To detect coronary arteries having all types of plaques, the thresholds, T_{blob}, T_{sheet}, and T_{noise} are experimentally determined to be 0.35, 0.25, and 0.0035, respectively. Figure 3.1 shows that the line similarity in (3.3) works well enough to restrict the search space of the subsequent constriction detection step.

In contrasted CT data for specific legions examination in tubular structures, the narrow linear region within the contrasted tubular structure has a high value of line similarity. However, the blob boundary also exhibits high line similarity, being falsely detected as a line. It is because the blob boundary, blurred by Gaussian prefiltering, is not regarded as a part of blob but as a line. To discriminate this, we analyze eigenvalue profiles along a line across the narrow linear and blob boundary regions (see Figure 3.2). The narrow linear region has a high rate of change in λ_2 and λ_3 but a low rate of change in λ_1. In contrast, the blob boundary region has a high rate of change in all three eigenvalues. Therefore, we use the rate of change in λ_1 for discriminating these two regions: low (or high) change rate in λ_1 indicates the narrow linear region (or the blob boundary region). Thus, the regions with higher eigenvalue gradients, regarded as the blob boundary, are excluded from the coronary artery (see (3.3), where the regions with eigenvalue gradient magnitude G_{λ_1} lower than the optimal threshold T_G are regarded as a line). Figure 3.3 and 3.4 show that the eigenvalue gradient magnitude successfully discriminates the blob boundary regions from areas with high line similarity: the blob boundary falsely detected as a line in Figure 3.3(c) (see the green regions in the left blob) and Figure 3.4 (a) (see the blue regions in the aorta) disappears in Figure 3.3 (d) and Figure 3.4 (b).

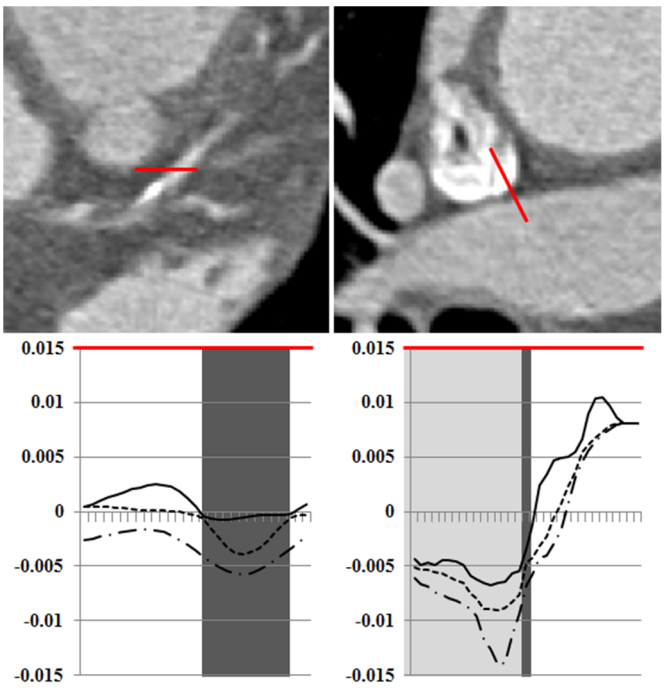

(a) (b)

Figure 3.2 Eigenvalue profiles of (a) narrow linear and (b) blob boundary regions. Upper row shows 2D slice images. Lower row shows eigenvalue profiles across the red line on the 2D slice images in the upper row. In narrow linear region, rates of change in λ_2 and λ_3 are high but a rate of change in λ_1 is low as in (a), whereas in blob boundary region, all three eigenvalues are high as in (b). (λ_1: solid line, λ_2: dashed line, λ_3: dashed-dotted line, dark grey area: detected as a line, light grey area: detected as a blob).

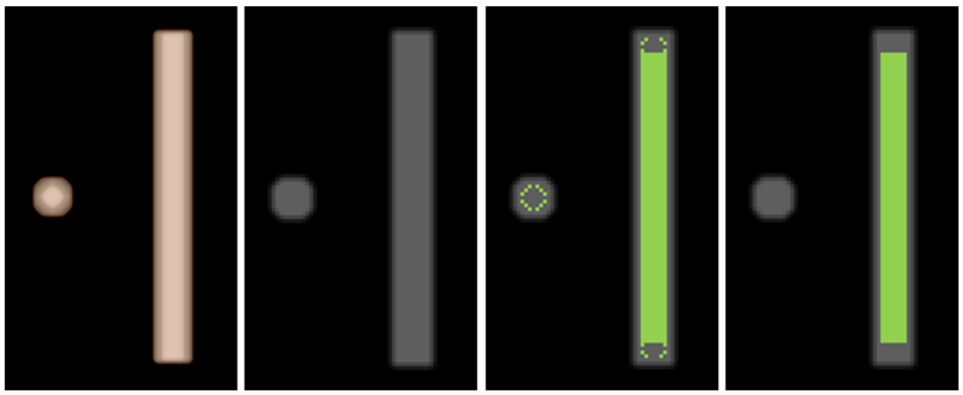

(a) (b) (c) (d)

Figure 3.3 Removal of blob boundary region based on eigenvalue gradient. (a) DVR of a 3D simulation phantom with a blob and a line. (b) Central slice of the phantom. (c) Without removal of blob boundary region, the boundary of the blob is falsely detected as a line. (d) With removal of blob boundary region ($T_G = 0.0025$), the false detection disappears. (The green represents the regions detected as a line).

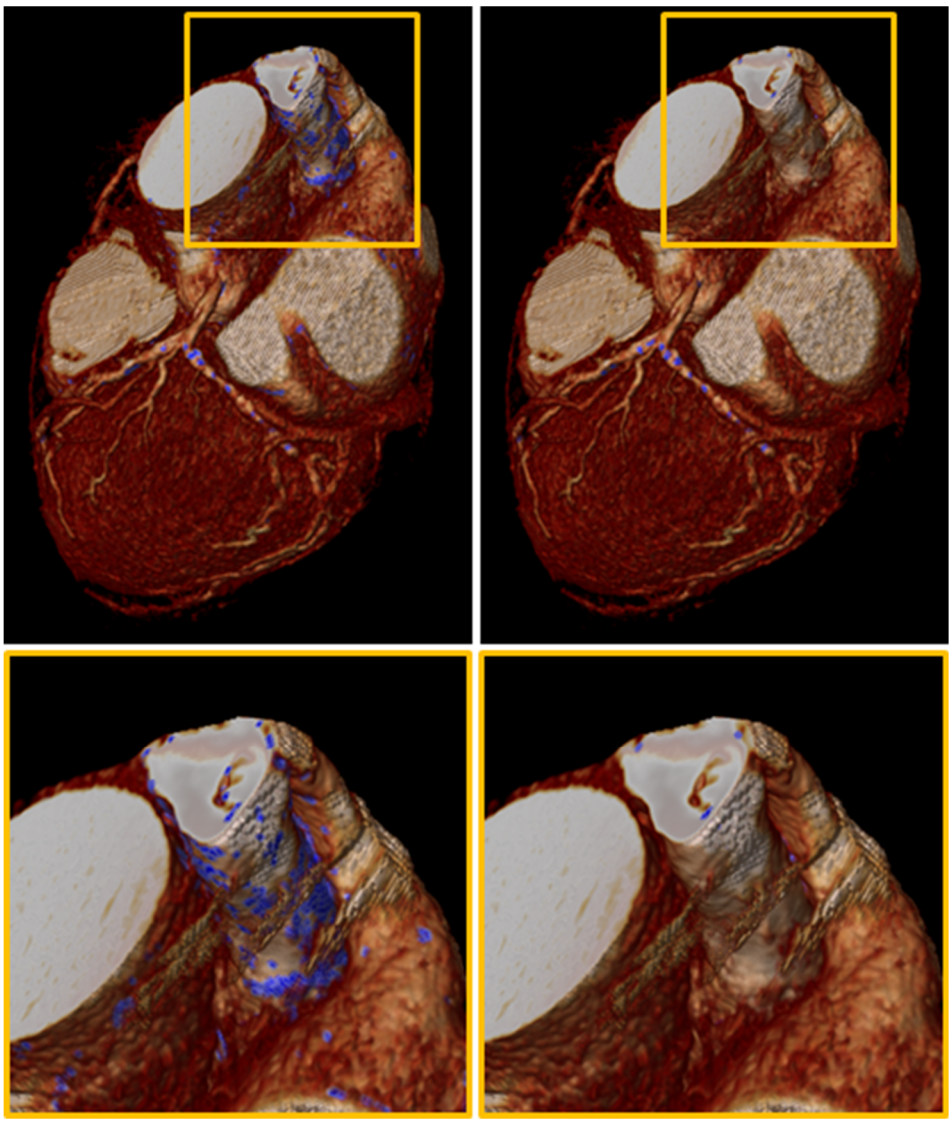

(a) (b)

Figure 3.4 Constriction detection (a) without and (b) with removal of blob boundary region based on eigenvalue gradient. The lower row shows close-up images of the orange rectangular region in the upper row. In (a), the boundary of the aorta is falsely detected as a line. (The blue represents the regions detected as a line).

3.3.3 Stenosis map computation

From the previously detected tubular structures (i.e., detected as a line), inner constricted regions (i.e., coronary artery stenosis) are detected. Constrictions are detected by using a constriction measure that is also derived from the Hessian matrix. In a similar manner as in the selection of optimal Gaussian scale for the coronary artery, we determine the optimal Gaussian scale for the stenosis. The severity of stenosis is assessed by the percentage of obstruction in the lumen diameter. The degree of stenosis severity – insignificant (< 50%) and significant (≥ 50%) – determines the treatment of CAD [56]. As mentioned in Section 3.1, the diameter of the coronary artery is about 9–15 voxels in coronary CT data with a spatial resolution of 0.3 mm. Significant stenoses are with at least 50% obstruction in the lumen diameter, and thus, the lumen with significant stenoses occupies at most 7.5 voxels (= 15 voxels × 50%). Therefore, we set the optimal Gaussian scale for the stenosis to be less than 1.875 (= 7.5/4). For the application to other kinds of constrictions, relevant constriction threshold (e.g., 50% obstruction in CCTA) can be used.

For accurate detection of constrictions (i.e., stenosis) within the tubular structures (i.e., coronary arteries), we devise a

constriction measure that quantifies how constricted compared to surrounding tubular structure. This constriction measure is applied only to the previously detected tubular structures. The stenosis is represented as a morphologically narrowed line. As described in Table 3.1, a line can be classified by $\lambda_3 \simeq \lambda_2 \ll \lambda_1 \simeq 0$. As a structure becomes less likely to be a line, $|\lambda_2|/|\lambda_3|$ decreases with negative λ_2 and λ_3. And as a line is getting morphologically narrowed, λ_1 increases and has a positive value [47]. Thus, the structure with $\lambda_1 \approx 0$ is regarded as a normal line rather than a morphologically narrowed line. Considering all these conditions, we propose the constriction measure as $M_{constrict}$ as follows:

$$M_{constrict} = \begin{cases} F_L \cdot F_N & if \quad \lambda_1 > 0 \quad and \quad \lambda_3 \le \lambda_2 < 0 \\ 0 & otherwise \end{cases}, \tag{3.7}$$

where

$$F_L = \exp\left(-\frac{(1-|\lambda_2|/|\lambda_3|)^2}{2\alpha^2}\right), \tag{3.8}$$

$$F_N = \exp\left(-\frac{(1-|\lambda_1|)^2}{2\beta^2}\right). \tag{3.9}$$

Figure 3.5 shows that the constriction measure in (3.7) quantifies the morphologically narrowed line well: constricted regions are

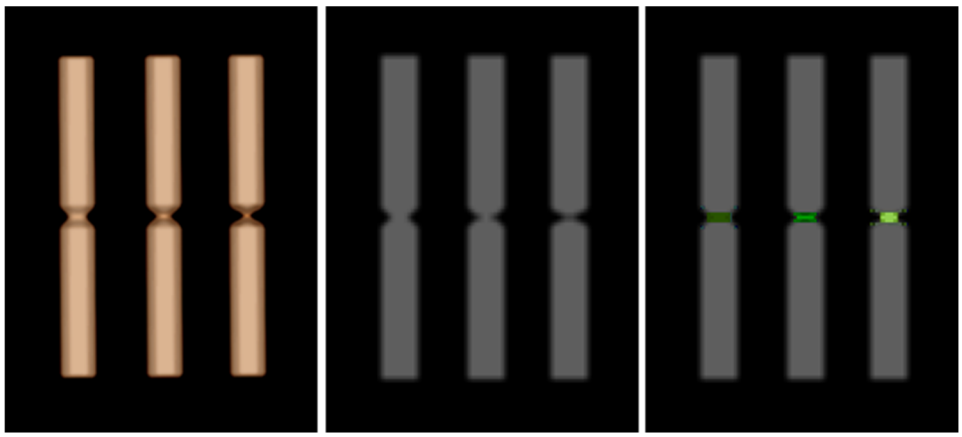

(a) (b) (c)

Figure 3.5 Constriction quantification. (a) DVR of a 3D simulation phantom with morphologically narrowed lines (left, 50% obstruction; middle, 70% obstruction; and right, 90% obstruction). (b) Central slice of the phantom. (c) Each line has a scalar value of its corresponding degree of constriction. The 50% obstructed line (left) has a lower value than 90% obstructed line (right). (The green represents the regions detected as a constriction. Higher degree of constriction is shown in brighter green).

detected and quantified by the proposed constriction measure, having scalar values of corresponding degree of constriction. The parameters α and β are experimentally set to be 0.115 and 0.185, respectively. As a result, we obtain the stenosis map in which each voxel has a scalar value (ranging from 0.0 to 1.0) of its corresponding degree of constriction $M_{constrict}$.

3.4 Stenosis-based classification

3.4.1 Overview

CCTA datasets can be visualized by using multi-planar reformation, maximum intensity projection, and/or DVR techniques. Specially, DVR intuitively displays and conveys complicated anatomical information of tortuous tubular structures. Among various DVR techniques, we employ a multi-volume ray-casting DVR. In order to saliently visualize constrictions (i.e., stenosis) within the tubular structures (i.e., coronary arteries), we propose a stenosis-based classification technique which uses a newly proposed transfer function reflecting the degree of constriction to color. When rendering the contrasted tubular structure (i.e., contrasted coronary arteries in CCTA), they are displayed with thigh opacity, often blocking the constrictions inside them. To resolve this problem, we propose a new opacity modulation strategy.

3.4.2 Constriction-encoded volume rendering

With the stenosis map, we have obtained the necessary information

to apply a stenosis-based transfer function. Among various DVR techniques, we employ a ray-casting DVR wherein a ray casted from an image plane traverses the volume data while sampling the intensity at a uniform (or non-uniform [2]) interval and compositing colors and opacities evaluated by a transfer function. At each sampling position P_i along a viewing ray, the color c_i and opacity α_i are computed as follows [57]:

$$\begin{aligned} c_i &= c_{i-1} + (1-\alpha_{i-1}) \cdot \alpha_{P_i} \cdot c_{P_i} \ , \\ \alpha_i &= \alpha_{i-1} + (1-\alpha_{i-1}) \cdot \alpha_{P_i} \ , \end{aligned} \tag{3.10}$$

where c_{i-1} and α_{i-1} are the previously accumulated color and opacity, respectively. c_{P_i} and α_{P_i} are the color and opacity contributions at the position P_i, which are defined as follows:

$$\begin{aligned} c_{P_i} &= TF_c(f_{P_i}) \ , \\ \alpha_{P_i} &= TF_\alpha(f_{P_i}) \ , \end{aligned} \tag{3.11}$$

where $\boldsymbol{TF_c}$ and $\boldsymbol{TF_\alpha}$ are transfer functions which assign color and opacity to the scalar value $\boldsymbol{f_{P_i}}$ at each position $\boldsymbol{P_i}$, respectively.

The stenosis map is rendered simultaneously with the input volume data by using multi-volume DVR. While a ray traverses both volume datasets simultaneously, it samples the intensity from the input volume data and the degree of constriction from the

stenosis map at a uniform interval. And it accumulates the color and opacity that can be evaluated using a transfer function proposed in (3.12) and (3.13).

To visualize the constrictions saliently, we propose a transfer function that reflects the degree of constriction to color:

$$c_{P_i} = \begin{cases} C_{constrict} & if \quad S_{map}(P_i) > T_{constrict} \\ TF_c(f_{P_i}) & otherwise \end{cases}, \tag{3.12}$$

where $S_{map}(P_i)$ is the degree of constriction at position P_i in the stenosis map, S_{map}, and $T_{constrict}$ is a threshold that influences the detection accuracy of constrictions. We optimally determine the threshold $T_{constrict}$ so that only stenosis regions are rendered with a predefined constriction color $C_{constrict}$. The sampling positions except for stenosis regions are assigned with colors evaluated by a user-defined transfer function for the input volume data.

3.4.3 Opacity modulation based on constriction

When rendering the contrasted tubular structures (i.e., contrasted coronary arteries in CCTA), they are displayed with high opacity, often blocking the constrictions inside them. As shown in Figure

3.6(a) and (b), although the proposed method accurately detects the constrictions (i.e., stenosis), opaque vessels hide the inner constrictions. To resolve this problem, we propose constriction-magnitude-based opacity modulation, motivated by the gradient-magnitude-based opacity modulation [23] that modifies the opacity according to the gradient magnitude for the boundary enhancement. We modulate the opacity based on the degree of constriction stored in the stenosis map as follows:

$$\alpha_{P_i} = TF_\alpha\left(f_{P_i}\right) \cdot m(P_i) \ , \tag{3.13}$$

where

$$m(P_i) = \delta + (1-\delta) \cdot S_{map}(P_i) \ . \tag{3.14}$$

The modulation factor $m(P_i)$ at position P_i is determined by the modulation base δ and the degree of constriction $S_{map}(P_i)$. By adjusting the modulation base δ, the users can interactively uncover occluded constrictions. Figure 3.6(c) and (d) show 3D renderings with two different values of δ. With smaller δ, areas inside the vessels are more revealed, the stenoses being more saliently visualized. This constriction-magnitude-based opacity modulation enables easy and intuitive adjustment of the transfer function when visualizing inner constrictions simultaneously with tubular structures.

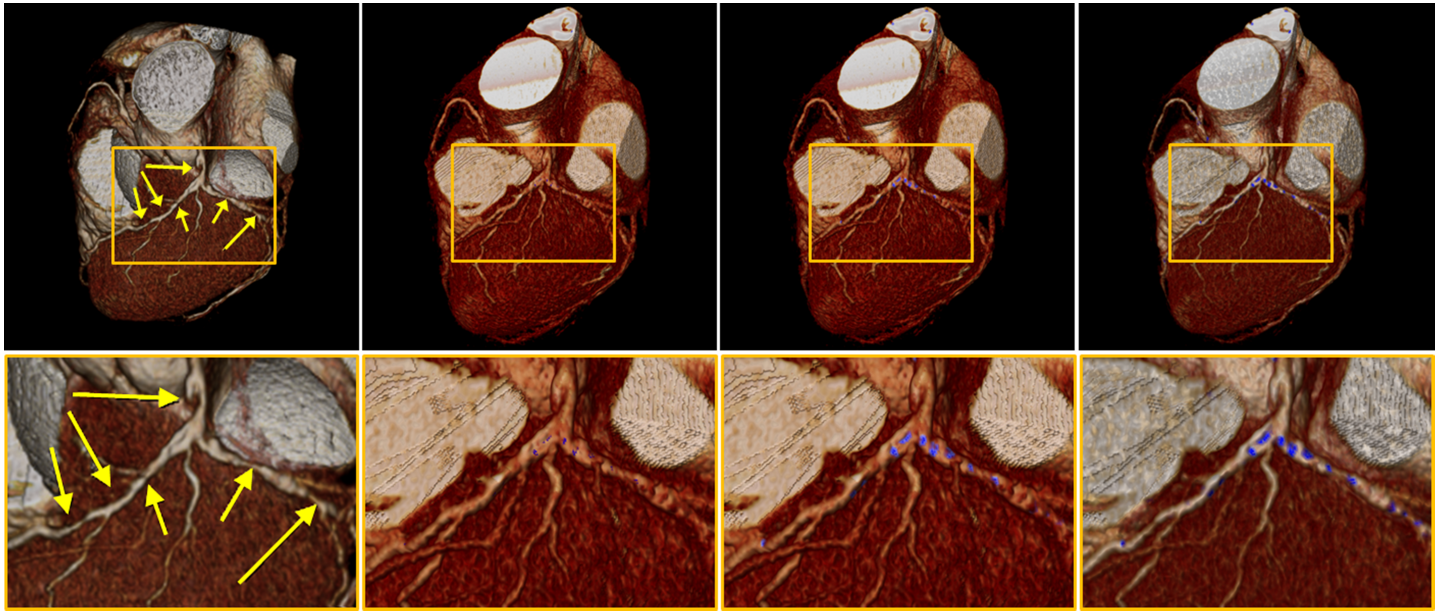

(a) (b) (c) (d)

Figure 3.6 Opacity modulation based on degree of constriction. (a) Reference standards (a radiologist manually identified stenoses with ≥ 50% blockage). (b) Without opacity modulation, some detected stenoses are invisible. (c) With opacity modulation ($\delta = 0.6$). (d) With opacity modulation ($\delta = 0.3$). As δ decreases from (c) to (d), areas inside the vessels are more revealed, the inner stenoses being more saliently visualized. The lower row shows close-up images of the orange rectangular region in the upper row.

3.5 GPU implementation

Our method computes the stenosis map in the pre-processing stage and provides an interactive 3D volume rendering using this pre-computed stenosis map (see Figure 3.7). Both stenosis map computation and data classification are implemented using GPU in separate HLSL programs (compute shader and pixel shader, respectively). To minimize the memory required by the stenosis map, we construct the stenosis map in a volume data of 8-bit float format. Although the 8-bit float has lower precision than 32-bit float, it preserves data precision enough to distinguish constricted tubular structures from other anatomical structures. The stenosis map computation is GPU-implemented by using a compute shader over two passes. The first pass computes eigenvalues for detecting tubular structures. The second pass detects tubular structures using the eigenvalues, and then computes the degree of constriction only for the voxels detected as tubular structures and stores them in the stenosis map. For multi-volume DVR, the stenosis map and the input volume data are both loaded in GPU memory. Data classification is done using both volume data by a GPU-based ray casting pixel shader. The proposed algorithms of stenosis map computation and data classification are implemented in Direct3D 11

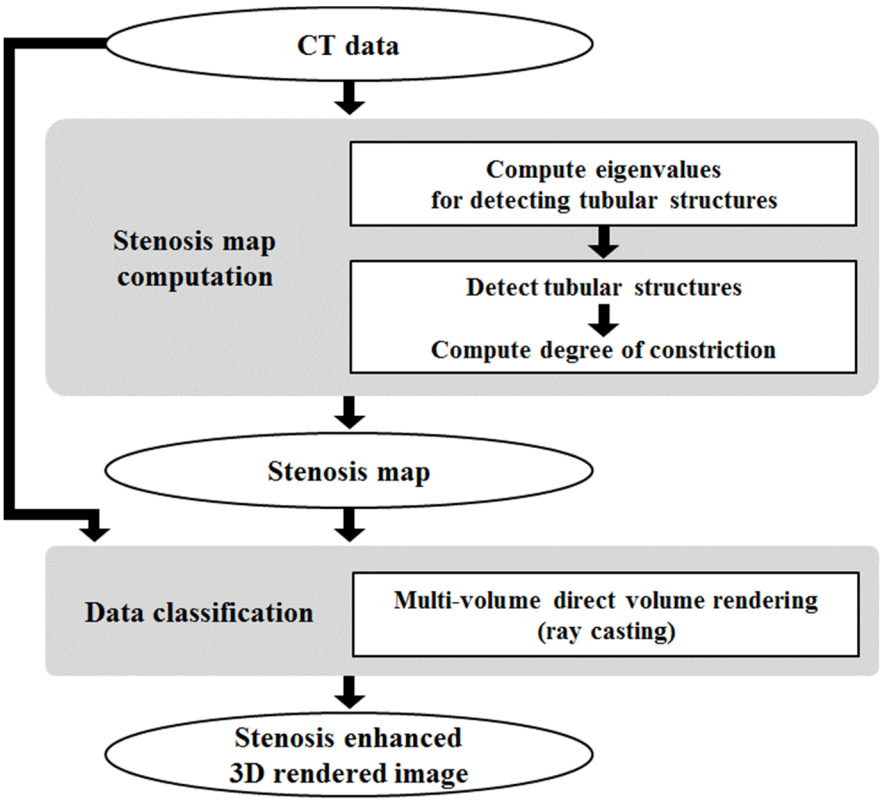

Figure 3.7 GPU implementation. The stenosis map is computed by using a compute shader over two passes in the pre-processing stage. Data classification is done using both the input volume data and the stenosis map by a GPU-based ray casting pixel shader.

and high level shading language on an NVIDIA GeForce GTX TITAN with 6 GB of memory.

3.6 Experimental results

3.6.1 Clinical data preparation

We evaluate the performance of the proposed method using ten clinical CCTA datasets from different patients. CT scanning was performed with a 256-row multi-detector CT scanner (iCT 256, Philips Medical Systems, Cleveland, OH). The number of images per scan ranged from 262 to 319. Each image has a matrix size of 512 × 512. The pixel size ranged from 0.29 to 0.42 mm, and the slice interval was all 0.45 mm.

For each CT dataset, a cardiac radiologist with 6 years of clinical experience manually specified coronary artery stenoses, assessed the degree of blockage of the coronary artery, and classified the type of plaque, which is the main cause of the blockage, into three types: non-calcified, calcified, and mixed plaques (see Figure 3.8). The purpose of the proposed method is to discriminatingly visualize coronary artery stenoses caused by all types of plaques. Thus, we evaluated the proposed method using the ten datasets that contain significant (≥ 50%) stenoses caused by at least one type of plaque (see Table 3.3).

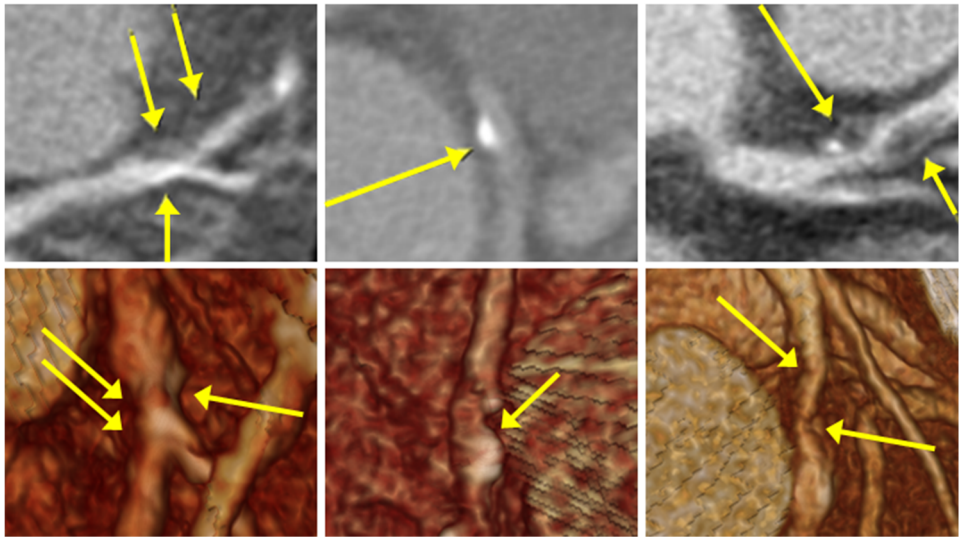

(a) (b) (c)

Figure 3.8 Three types of plaque [58]. (a) Non-calcified plaque has low density compared to contrast-enhanced vessels without any visible calcification. (b) Calcified plaque was defined as plaque having calcification (≥ 130HU) in more than 50% of the entire volume. (c) Mixed plaque was defined as plaque having calcification in < 50% of the entire volume. The upper and lower rows show 2D slices and 3D rendered images, respectively.

3.6.2 Qualitative evaluation

We qualitatively evaluate the proposed constriction visualization method by comparing it with the conventional classification [59]. Figure 3.9 shows the 3D renderings of a CCTA dataset (dataset #1)

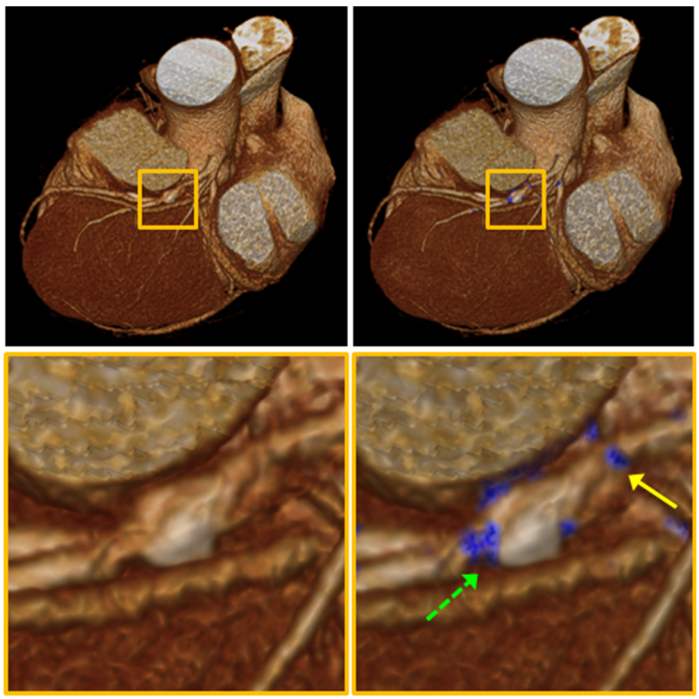

(a) (b)

Figure 3.9 3D rendered images using (a) conventional classification and (b) proposed stenosis-based classification. Regions constricted by plaques, which are invisible (a), are clearly visualized in blue in (b). The lower row shows close-up images of the orange rectangular region in the upper row (green dashed arrow: calcified plaque, yellow solid arrow: non-calcified plaque).

containing ≥ 80% coronary artery stenoses caused by both non-calcified and calcified plaques. Whereas the plaques are not distinguishable in the conventional method (Figure 3.9 (a)), the regions constricted by plaques are clearly visualized in a predefined color (blue) with the proposed method (Figure 3.9 (b)).

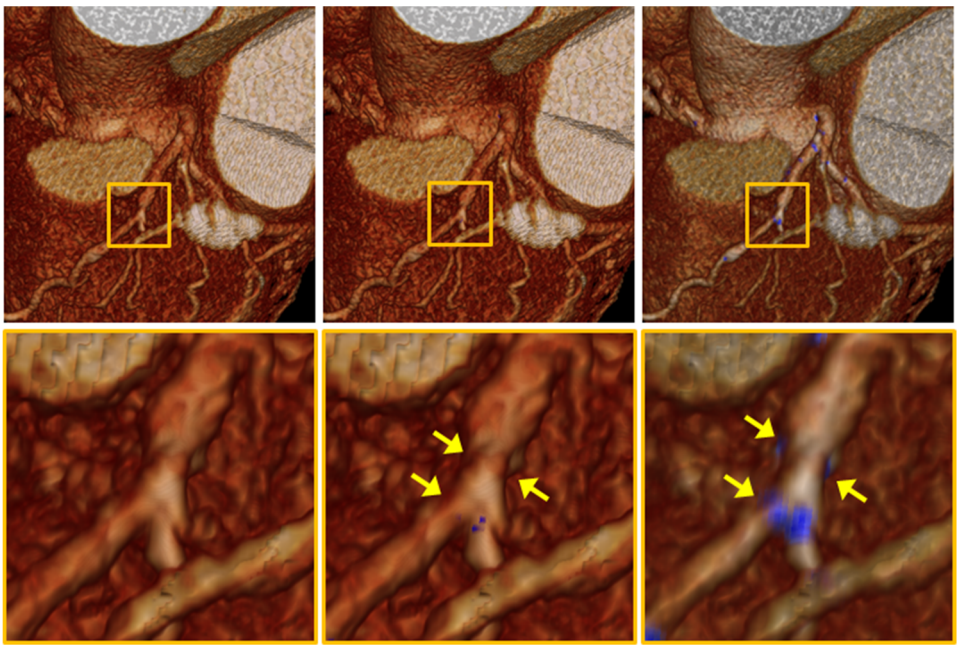

(a) (b) (c)

Figure 3.10 3D rendered images using (a) conventional classification and proposed stenosis-based classification with (b) $\delta = 1.0$ and (c) $\delta = 0.4$ in (3.14). The proposed opacity modulation based on degree of constriction enables a clear visualization of the inner stenoses, where smaller δ shows more inner stenoses. The lower row shows close-up images of the orange rectangular region in the upper row (yellow arrow: mixed plaque).

Figure 3.10 shows the 3D renderings of a CCTA dataset (dataset #7) containing ≥ 70% coronary artery stenosis caused by mixed plaques. The stenoses are almost invisible in the conventional method (Figure 3.10 (a)). The proposed method detects the stenoses accurately; however, the contrast-enhanced

vessels, which are opaquely rendered with a typical transfer function for the coronary artery visualization, usually hide the inner stenoses (Figure 3.10 (b)). The proposed opacity modulation modifies the opacity based on the degree of constriction, delivering a clear visualization of the inner stenosis (Figure 3.10 (c)).

In the conventional classification, it is tedious or very difficult to specify an appropriate transfer function which visually distinguishes all features of interests. Not rarely, it is almost impossible to visualize a feature of interest (e.g., stenosis caused by non-calcified or mixed plaques) inside a structure that should be simultaneously rendered (e.g., coronary artery). In contrast, the proposed stenosis-based classification enables the salient visualization of constrictions within a tubular structure that have very poor visibility in the conventional classification.

3.6.3 Quantitative evaluation

We quantitatively validate how accurately the stenosis map encodes constrictions. As described in Section 3.6.1, a cardiac radiologist with 6 years of clinical experience manually specified coronary artery stenoses in each of the ten datasets. For each dataset, the radiologist manually identified stenoses with ≥ 50% blockage. In

this way, we obtained the manually classified stenoses that serve as the ground truth for the accuracy assessment of the proposed method. The cardiac radiologist assessed the images twice to avoid intra-observer disagreement.

We evaluated the accuracy of the automatic stenosis classification of the proposed method in terms of two different factors as follows:

$$E_{FP} = num\{(\Omega_{All} - \Omega_{Manual}) \cap \Omega_{Auto}\} \ , \\ E_{FN} = num\{\Omega_{Manual} \cap (\Omega_{All} - \Omega_{Auto})\} \ , \tag{3.15}$$

where Ω_{Manual} and Ω_{Auto} are the regions of manually and automatically classified stenosis and Ω_{All} is the whole regions of a CCTA dataset. The false positive error E_{FP} is the number of stenosis regions classified automatically but not classified manually, relating to the specificity. The false negative error E_{FN} is the number of stenosis regions classified manually but not classified automatically, relating to the sensitivity.

Table 3.3 summarizes the stenosis classification errors for the ten datasets. E_{FN} was 0 for all datasets, indicating that the proposed method did NOT miss any coronary artery stenosis. Although E_{FP} seemed to be relatively large, the number of regions incorrectly classified as stenosis was very small compared to that

of whole regions in a CCTA dataset. In addition, about 30% of these incorrect regions were non-cardiovascular regions (e.g., aorta), and thus, they could be easily excluded. Therefore, the over-classification of stenosis did not degrade the overall diagnostic performance when cardiac radiologists diagnose coronary artery stenoses in CCTA.

Our method generates the stenosis map in the pre-processing step while computing the Hessian matrix and its eigenvalues at each

Table 3.3 Accuracy assessment result of stenosis classification

	Dataset	E_{FP}	E_{FN}
1	Proximal LAD 80% stenosis, non-calcified and calcified plaques	4	0
2	LM, proximal LAD, proximal LCX 50% stenosis, calcified plaque	7	0
3	Proximal LAD 70% stenosis, calcified plaque	3	0
4	LM, proximal LAD 70% stenosis, calcified plaque	6	0
5	Proximal LAD 80% stenosis, mixed plaque	9	0
6	Proximal LAD 80% stenosis, mixed plaque	3	0
7	Mid LAD 70% stenosis, mixed plaque	6	0
8	Proximal LAD 70% stenosis, calcified plaque Distal LCX 70% stenosis, mixed plaque	7	0
9	Proximal to mid LAD 80% stenosis, non-calcified plaque	12	0
10	Proximal to mid LAD 90% stenosis, calcified plaque	1	0

voxel of a CCTA dataset. Such per-voxel computation was accelerated using parallel processing on a GPU in our implement-ation. The stenosis map computation time, averaged over multiple tests for all ten datasets, was 47.42 ± 3.24 s, and the average rendering speed was 42.6 ± 1.22 fps.

3.6.4 Comparison with previous methods

We compared the result of our method with those of 11 recently proposed methods, which were presented at MICCAI 2012 workshop, '3D Cardiovascular Imaging: a MICCAI segmentation challenge' [41]. A database for this workshop consists of 48 multi-center multi-vendor CCTA datasets. Among of them, 18 CCTA datasets have reference standard quantification results obtained from the coronary angiography procedure and consensus reading of CCTA. We measured and compared the detection accuracy results using these 18 CCTA datasets with the corresponding reference standard from coronary angiography.

For the reference standard generation, one experienced cardiologist identified and analyzed all the coronary artery segments [41]. The stenosis detection method is evaluated using

the metrics described in [41] – the sensitivity and the positive predictive value (PPV) as follows:

$$\text{Sensitivity} = \frac{\text{TP}}{\text{TP} + \text{FN}}\ , \tag{3.16}$$

$$\text{PPV} = \frac{\text{TP}}{\text{TP} + \text{FP}}\ , \tag{3.17}$$

where the true positive (TP) means that both the reference standard and the algorithm stenosis/segment have a grade ≥ 50%. The false negative (FN) means that the reference standard stenosis/segment has a grade ≥ 50% while the algorithm stenosis/segment has a grade < 50%. The false positive (FP) means that the reference standard stenosis/segment has a grade < 50% while the algorithm stenosis/segment has a grade ≥ 50%.

Table 3.4 shows the accuracy comparison results of the proposed method with 11 previous methods whose accuracy was reported in [41]. The accuracy was measured using the identical 18 CCTA datasets. As shown in Table 3.2, the proposed method shows the highest sensitivity of 92% for the detection of stenosis among of them. Our method did not miss any coronary artery stenosis except the occluded stenosis. Although our method shows a

Table 3.4 Accuracy comparison results with previous methods

Methods	Category	Sensitivity	PPV
Cetin and Unal [15]	Min. user	68	49
Duval *et al.* [60]	Automatic	68	21
Mohr *et al.* [61]	Automatic	72	25
Shahzad *et al.* [62]	Min. user	48	63
Broersen *et al.* [63]	Automatic	36	39
Öksüz *et al.* [64]	Min. user	36	**64**
Melki *et al.* [65]	Automatic	60	20
Wang *et al.* [66]	Automatic	40	30
Lor and Chen [67]	Min. user	44	48
Eslami *et al.* [68]	Min. user	56	19
Flórez-Valencia *et al.* [69]	Min. user	24	11
Proposed method	Automatic	**92**	17

Note. The maximum value of each column is marked in bold. 'Min. user' represents minimal user interaction.

relatively low PPV which indicates an increase in the number of false positives, considering the trade-off between sensitivity and specificity of a detection algorithm, the over-detection of lesions would benefit patients better than the miss of lesions.

3.6.5 Parameter study

The parameter study described in this section will show an easy-to-follow procedure to determine major parameters in the proposed method when applied to other constricted tubular structures. We evaluated the effects of major parameters on the constriction (i.e., stenosis) detection accuracy using another nine test datasets.

At the stage of Gaussian prefiltering, the optimal size of neighboring window is as important as the optimal Gaussian scale. The neighboring window size determines the local range for the localized structure analysis, and thus, it directly influences the constriction detection accuracy. The proposed method involves two steps of localized structure analysis with different target objects of coronary artery and stenosis. Each analysis uses the optimal Gaussian scale corresponding to its target object. For each of these two localized structure analyses, we evaluated the final constriction detection error, computed by averaging false positive errors E_{FP} and false negative errors E_{FN} across all the nine test datasets.

While varying the neighboring window size from 9×9×9 to 15×15×15 in the first step of coronary artery detection, the final constriction detection error was computed. The optimal neighboring window size was determined to be 13×13×13 with the smallest

Table 3.5 Constriction detection error with varying neighboring window size for coronary artery detection

Neighboring window size		9^3	11^3	$\mathbf{13^3}$	15^3
Constriction detection error (# of incorrectly detected region)	E_{FP}	4.3	0.6	5.8	12.9
	E_{FN}	7.9	3.1	**0.0**	0.8

Note. Neighboring window size A^3 represents $A \times A \times A$.

Table 3.6 Constriction detection error with varying neighboring window size for stenosis detection

Neighboring window size		5^3	7^3	$\mathbf{9^3}$	11^3
Constriction detection error (# of incorrectly detected region)	E_{FP}	0.0	0.7	5.8	15.5
	E_{FN}	8.1	4.9	**0.0**	0.1

Note. Neighboring window size A^3 represents $A \times A \times A$.

false negative error of 0.0 (see Table 3.5). Similarly, while varying the neighboring window size from 5×5×5 to 11×11×11, the optimal neighboring window size in the second step of stenosis detection was determined to be 9×9×9 with the smallest false negative error of 0.0 (see Table 3.6).

The parameter T_{blob}, T_{sheet}, and T_{noise} in (3.3) for the detection of tubular structures (i.e., coronary arteries) influence the final constriction detection since they determine the search space of

the subsequent stenosis map computation. While varying each threshold, we assessed the final constriction detection error as in the previous optimal window size determination using the nine test datasets, and then determined an optimal value.

From 0.25 to 0.45, the threshold T_{blob} was optimally determined to be 0.35 with the smallest false positive error of 4.3 and the false negative error of 0.0 (see Table 3.7). Through the assessment of the threshold T_{sheet} from 0.15 to 0.9, T_{sheet} (smaller T_{sheet} leads to higher false positive) was found to minimally affect the constriction detection error. With T_{sheet} smaller than 0.75, the final constriction detection error was all identical as the blob boundary region removal using the eigenvalue gradient also removed the false positive regions possibly detected with T_{sheet} < 0.75. With T_{sheet} > 0.75, the false negative error increased. Thus, we set T_{sheet} to be 0.25, one value < 0.75. From 0.0025 to 0.0045, the threshold T_{noise} was optimally determined to be 0.0035 with the smallest false positive error of 4.3 and the false negative error of 0.0 (see Table 3.8).

We introduced the eigenvalue gradient magnitude G_{λ_1} in (3.3) for excluding the blob boundary regions which are falsely detected as tubular structures. From 0.0005 to 0.003, the threshold T_G was optimally determined to be 0.001 with the smallest false positive error of 5.8 and the false negative error of 0.0 (see Table 3.9).

Table 3.7 Constriction detection error with varying threshold T_{blob}

Threshold T_{blob}		0.25	0.3	**0.35**	0.4	0.45
Constriction detection error (# of incorrectly detected region)	E_{FP}	3.0	4.0	**4.3**	6.7	9.3
	E_{FN}	1.3	0.7	**0.0**	0.0	0.0

Table 3.8 Constriction detection error with varying threshold T_{noise}

Neighboring window size		0.0025	**0.0035**	0.0045
Constriction detection error (# of incorrectly detected region)	E_{FP}	16.7	**4.3**	1.7
	E_{FN}	0.0	**0.0**	2.7

Table 3.9 Constriction detection error with varying eigenvalue gradient threshold T_G

Neighboring window size		0.0005	**0.001**	0.002	0.003
Constriction detection error (# of incorrectly detected region)	E_{FP}	2.7	**5.8**	9.5	10.9
	E_{FN}	1.6	**0.0**	0.0	0.0

Chapter 4. Interactive Multi-Dimensional Transfer Function Using Adaptive Block Based Feature Analysis

4.1 Overview

We also propose a data exploration method based on parallel coordinates. Our data exploration method uses the statistical and texture features to define a new multi-dimensional transfer function which is able to achieve the desired classification of objects in direct volume rendering. First, we extract the statistical features (i.e., mean value and standard deviation) using adaptive growing technique which also extrudes the relative size of the local feature at each voxel. Second, we calculate the texture features (i.e., entropy and homogeneity) using adaptive block based GLCM which is defined based on the previously computed relative size at each voxel. Finally, we define a new multi-dimensional transfer function using previously computed statistical and texture features, which incorporates parallel coordinate wherein each voxel is represented as a polyline with parallel axes of individual multi-

dimensional features.

4.2 Extraction of statistical features

Prior to analyzing the texture features, we first extract the statistical features (i.e., mean value and standard deviation) using the adaptive growing technique. We employ the adaptive growing approach of Haidacher *et al.* [18] which iteratively grow a spherical neighborhood by increasing the radius by one voxel in each step. We briefly review this approach as follows; and refer interested readers to [18] for details.

In the following review, we use two different notations for the statistical properties. The mean value μ_r and the standard deviation σ_r for a certain radius r, are the estimations for the statistical

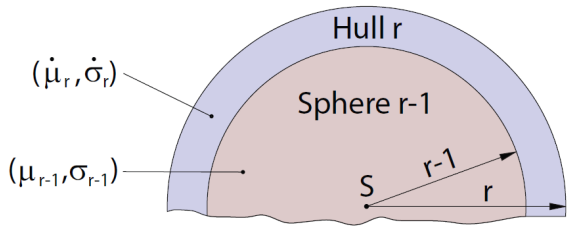

Figure 4.1 Mean value and standard deviation for the sphere and the outer hull. Image courtesy of Haidacher *et al.* [18].

properties of all points within a sphere of radius r. $\dot{\mu}_r$ and $\dot{\sigma}_r$ are the statistical properties of the points in the outer hull of the sphere (see Figure 4.1). This method compares for each growing step if the newly grown hull still belongs to the same material. Figure 4.2 shows the processing steps for each growing step. In each growing step, the statistical properties of a larger region are considered. Since the statistical properties of sphere $r-1$ are already known, those of the additional points in the hull (i.e., $\dot{\mu}_r$ and $\dot{\sigma}_r$) are estimated. Before applying a similarity test between the statistical properties of the hull and the inner sphere, it must be ensured that the distribution of data values in the hull is normally distributed.

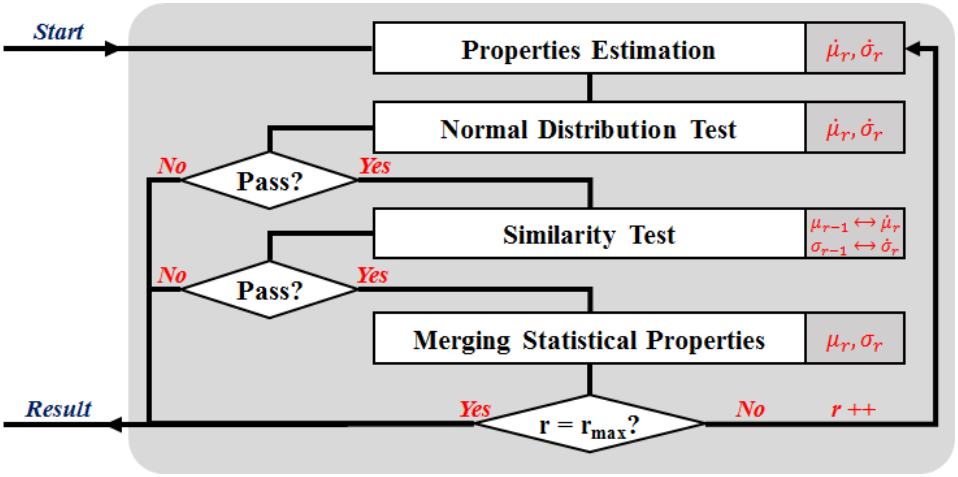

Figure 4.2 Adaptive growing technique for the extraction of the statistical features (i.e., mean value and standard deviation). Image courtesy of Haidacher *et al.* [18].

This is necessary because the similarity test is based on normal distributions. Among various normality tests in statistics, they chose the Jarque–Bera test [70] which uses the third–order moment (i.e., skewness) and the fourth–order moment (i.e., kurtosis). If this test is passed, the similarity test is continued. The similarity test detects whether the hull is still part of the same material as the sphere $r-1$ using a generalized form of the student's t–test known as the Welch's t–test [71]. If the statistical properties have passed the normal–distribution test and the similarity test, the material in the outer hull still is considered the same as that in the sphere $r-1$. Thus, the statistical properties of both areas are merged together. These merged statistical properties are used in the next growing step of the adaptive growing technique. The loop is terminated when the normal–distribution test or the similarity test fails or when the maximum radius (six in case of our method) is reached. Additionally, this adaptive growing technique extrudes the radius at which the loop is terminated. This radius is considered the relative size of the local feature at each voxel, that is the size of statistically homogeneous regions. Figure 4.3 show the result of the adaptive growing technique, which is the radius at which the loop is terminated with maximum radius 6. Since the adaptive growing approach of

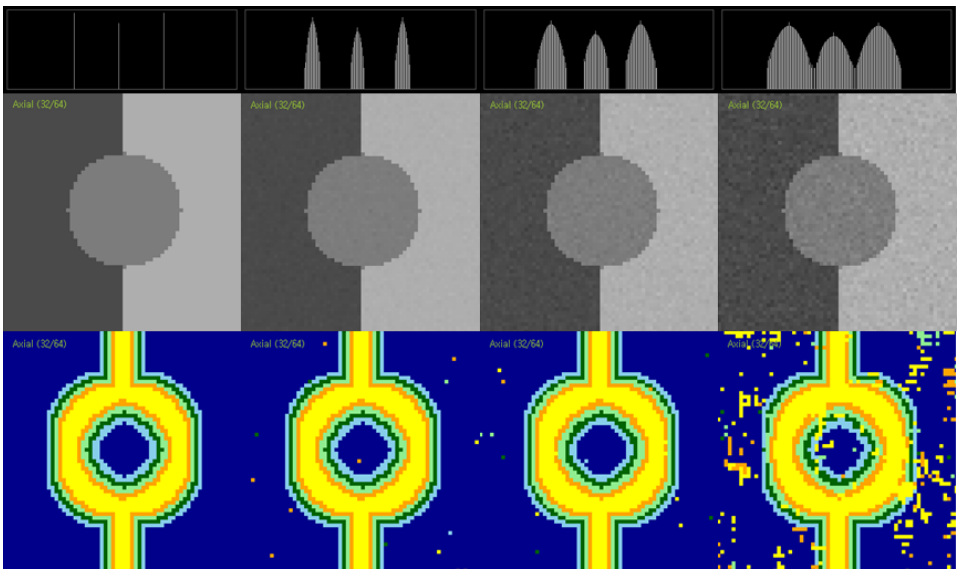

(a) (b) (c) (d)

Figure 4.3 Radius at which the loop of the adaptive growing technique of Haidacher *et al.* [18] is terminated. Upper row shows histograms of synthetic datasets (a) without and (b)−(d) with Gaussian noise ((b)$\sigma = 2$, (c)$\sigma = 4$, (d)$\sigma = 6$). Middle row shows 2D slices images. Lower row shows the result of adaptive growing technique, that is the radius at which the loop is terminated with the maximum radius 6 (yellow: $r = 1$, orange: $r = 2$, light green: $r = 3$ dark green: $r = 4$, light blue: $r = 5$, dark blue: $r = 6$).

Haidacher *et al.* [18] deals with noise in the data, statistically homogeneous regions are successfully detected regardless of presence of noise; and an extruded radius can be considered the relative size of the local feature at each voxel.

4.3 Extraction of texture features

Using the previously computed relative size of the local feature of each voxel, texture features (i.e., entropy and homogeneity) are calculated. Texture is one of the important characteristics used in identifying objects or regions of interest in an image, and contains important information about the structural arrangement of surfaces [72]. In statistical texture analysis, texture features are computed from the statistical distribution of observed combinations of intensities at specified positions relative to each other in the image [73]. Depending on the number of intensity values in each combination, statistical texture analysis methods can be further classified into first−, second−, and higher−order statistics. Among various methods for statistical texture analysis, we employ GLCM which is a way of extracting second−order statistical texture features.

GLCM is a matrix that is defined by calculating how often pairs of pixel with specific values occur at a given offset. For an image containing g different gray levels, $g \times g$ GLCM, parameterized by an offset $(\Delta x, \Delta y)$, is defined over an $N \times M$ image I as follows:

0	0	1	1
0	0	1	1
0	2	2	2
2	2	3	3

(a)

Gray tone	0	1	2	3
0	#(0,0)	#(0,1)	#(0,2)	#(0,3)
1	#(1,0)	#(1,1)	#(1,2)	#(1,3)
2	#(2,0)	#(2,1)	#(2,2)	#(2,3)
3	#(3,0)	#(3,1)	#(3,2)	#(3,3)

(b)

4	2	1	0
2	4	0	0
1	0	6	1
0	0	1	2

(c)

4	1	0	0
1	2	2	0
0	2	4	1
0	0	1	0

(d)

6	0	2	0
0	4	2	0
2	2	2	2
0	0	2	0

(e)

2	1	3	0
1	2	1	0
3	1	0	2
0	0	2	0

(f)

Figure 4.4 GLCM is a matrix that is defined by calculating how often pairs of pixel with specific values occur at a given offset. (a) Test image. (b) General form of GLCM. (c)–(f) GLCM with varying orientations and the fixed radius. (c) $\theta = 0^{\circ}$ and $r = 1$. (d) $\theta = 45^{\circ}$ and $r = 1$. (e) $\theta = 90^{\circ}$ and $r = 1$. (f) $\theta = 135^{\circ}$ and $r = 1$. Image courtesy of [72].

$$\mathrm{GLCM}(i,j) = \sum_{x=1}^{N}\sum_{y=1}^{M}\begin{cases}1, & if\ \ I(x,y)=i\ \ and\ \ I(x+\Delta x, y+\Delta y)=j \\ 0, & otherwise\end{cases}, \quad (4.1)$$

where $I(x,y)$ indicates the pixel value at the spatial position (x,y). Figure 4.4 (a) presents a test image with four different gray levels 0 through 3. Figure 4.4 (b) shows a generalized GLCM where $\#(i,j)$ stands for the number of times the pair of gray levels i and j have been occurred. Instead of the offset $(\Delta x,\ \Delta y)$, GLCM can also be parameterized in terms of a radius r and an orientation θ. The four GLCM with varying orientations ($\theta = 0^{\circ}$, 45°, 90°, and 135°) and the fixed radius equal to 1 are shown in Figure 4.4 (c)−(f). Displacement value (i.e., radius) equal to the size of the texture element improves classification [72]. The proposed method uses a moving window over the image; the size of neighboring window is determined by the previously computed relative size of the local feature at each voxel. Since the texture features are extracted based on the neighborhood within the same material, the adaptive block based GLCM enhances the accuracy of texture analysis.

The texture features are calculated by extracting the statistical measures from GLCM [74]. The features generated using this technique include contrast, entropy, homogeneity, etc. Table 4.1 summarizes some of the texture features from GLCM we have explored.

Table 4.1 Texture features from GLCM

Contrast	$\sum_i \sum_j \lvert i-j \rvert^2 GLCM(i,j)$
Correlation	$\sum_i \sum_j GLCM(i,j) \frac{(i-\mu)(j-\mu)}{\sigma^2}$
Energy	$\sum_i \sum_j GLCM(i,j)^2$
Homogeneity	$\sum_i \sum_j \frac{GLCM(i,j)}{1+\lvert i-j \rvert}$
Entropy	$\sum_i \sum_j GLCM(i,j) \log GLCM(i,j)$

Note. μ and σ represent mean value and standard deviation, respectively.

4.4 Multi-dimensional transfer function design using parallel coordinates

After the statistical and texture features have been extracted, they are used to define a new multi-dimensional transfer function, which incorporates parallel coordinate; it is a popular technique for visualizing and analyzing high-dimensional data in information visualization. In our system, each voxel is represented as a polyline

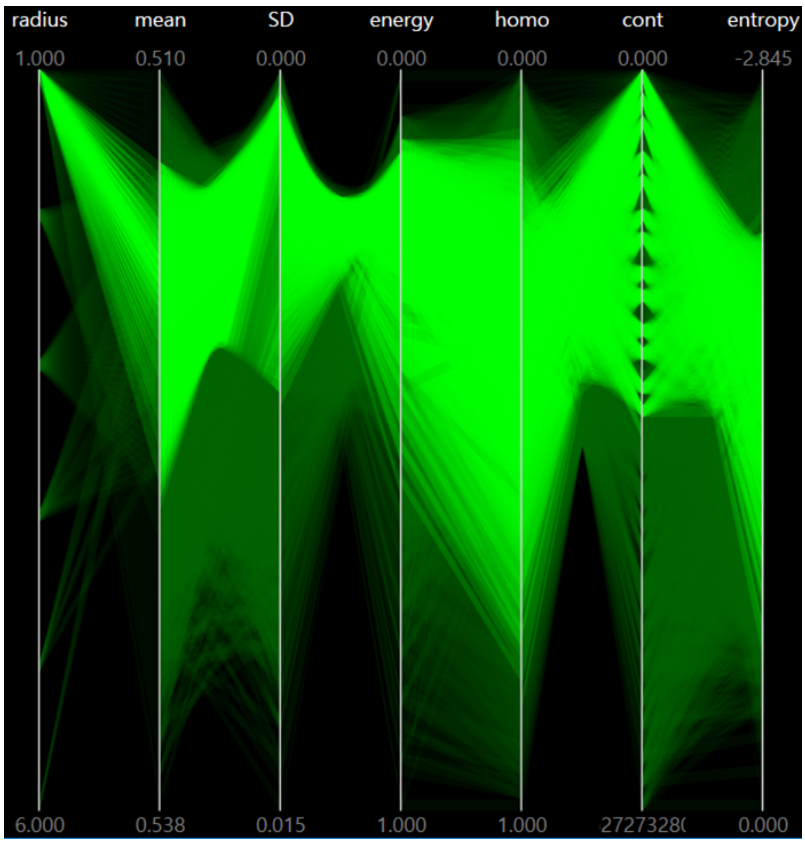

Figure 4.5 Multi-dimensional transfer function design using parallel coordinates. In the parallel coordinated, each vertical axis corresponds to computed individual features (i.e., statistical and texture features) and each data element is represented by one polyline with vertices on the parallel axes; the position of the vertex on the i th axis corresponds to the i th coordinates of the data element.

with parallel axes of individual multi-dimensional features (see Figure 4.5). As mentioned in Section 1.1.3, the parallel coordinates allow the user to interact with the data in many ways. We present three specific ways to use our multi-dimensional transfer function

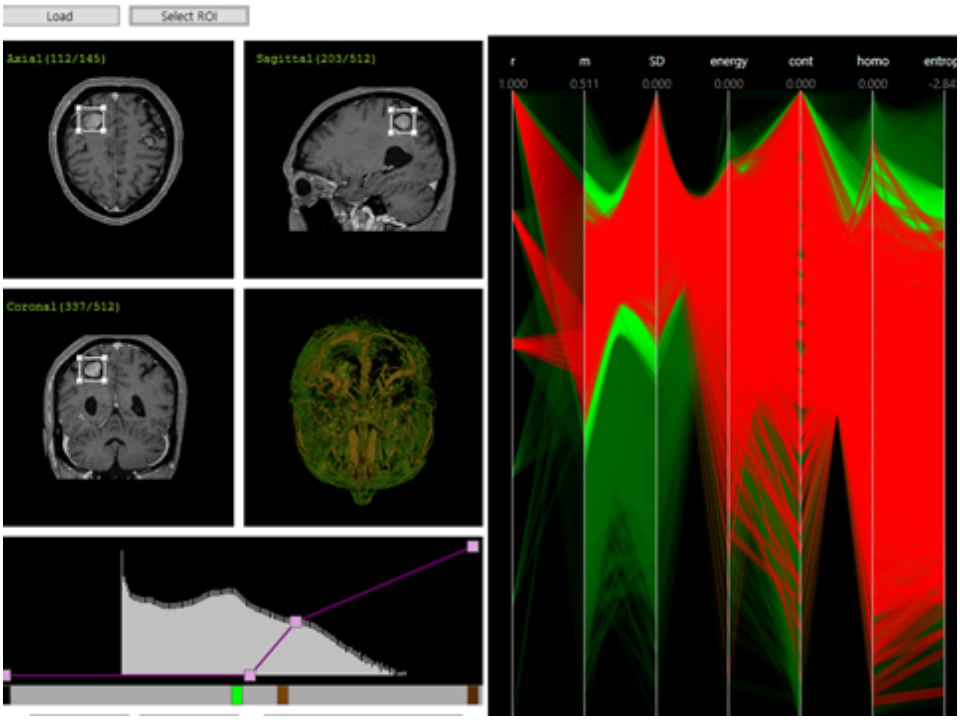

Figure 4.6 Cube-based selecting user interface. The user specifies a ROI using a cube-based selecting user interface in the MPRs. By highlighting the data of the selected ROI in the parallel coordinates, the user can easily analyze the statistical and texture features of them.

based on parallel coordinates to enable the effective exploration of large and complex datasets. First, the user can specify a region of interest (ROI) using a cube-based selecting user interface in the multi-planar reformations (MPRs). MPRs are 2D reformatted images that are reconstructed secondarily in arbitrary planes from the stack of axial images [75]. By highlighting the data of the selected ROI in the parallel coordinates, the user can easily analyze the statistical and texture features of them (see Figure 4.6).

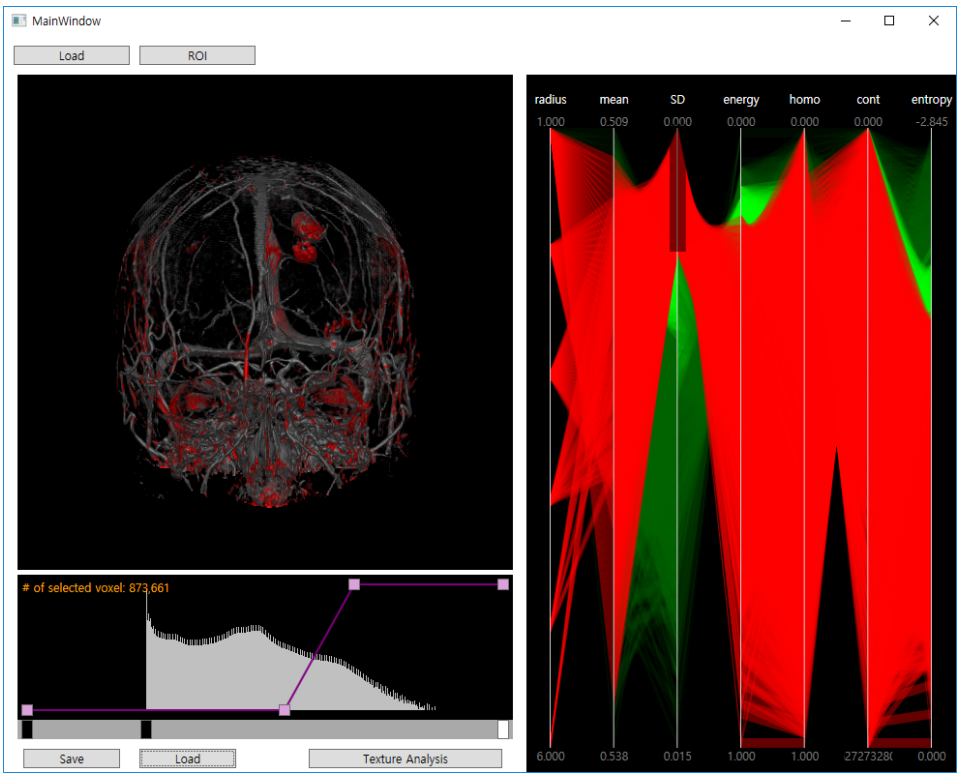

Figure 4.7 Brushing user interface. The user selects a subset of the data by brushing on the SD axis from 0.0 to 0.0025. By coloring the selected set of the data in the volume rendering, the user can identify and analyze patterns revealed in the parallel coordinates.

Second, the user can select a subset of the data by using a brushing operation in the parallel coordinates. By coloring the data in the volume rendering, the selected set of the data can be clearly visualized, the user can identify and analyze the data corresponding to patterns revealed in the parallel coordinates (see Figure 4.7). Finally, the user can specify a value k which is the number of structures to discriminate. By using $k-$means clustering, the data is

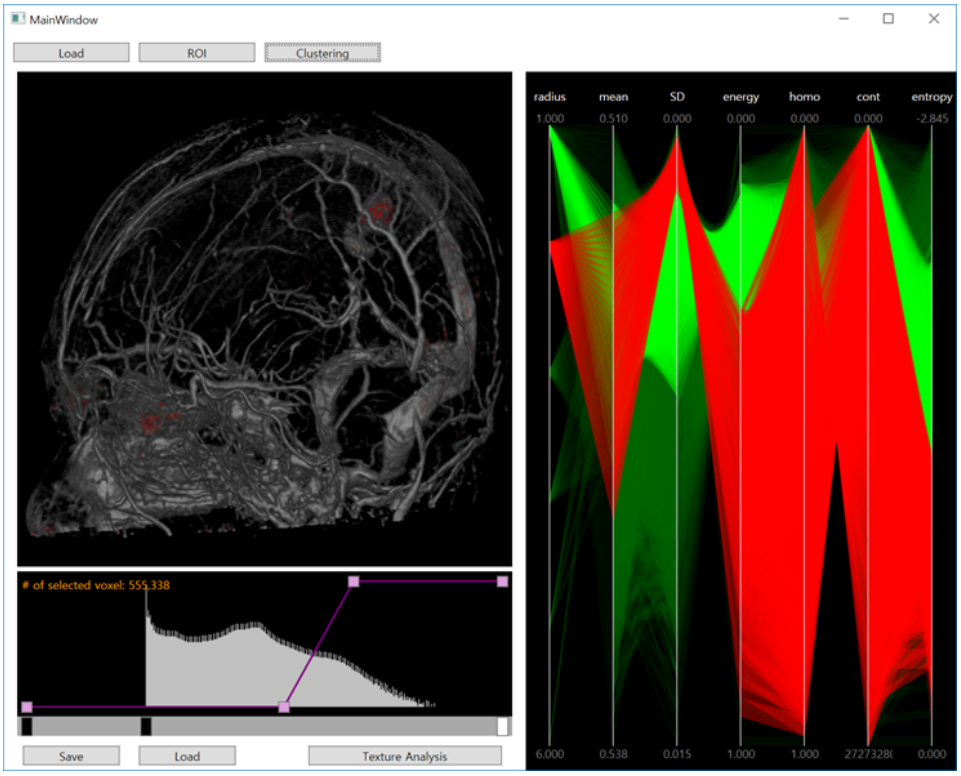

Figure 4.8 Automatic classification. The user specifies a value k which is the number of structures to discriminate. By using k −means clustering, dominant features contained within the volumetric dataset is colored (highlighted) in both volume rendering and parallel coordinates.

automatically classified into k groups, and the data of the largest group is colored (highlighted) in both volume rendering and parallel coordinates (see Figure 4.8). This automatic classification is useful to understand dominant features contained within the volumetric dataset.

4.5 Experimental results

The parallel coordinate representation is used as a tool to help users in specifying a transfer function to classify or segment large and complex dataset. In order to demonstrate the practical efficacy of our data exploration method, we present a mechanism for data exploration with a new transfer function space. We illustrate this mechanism step-by-step with a dataset of brain tumor MR scans in Figure 4.9. The user begins with classifying the volume dataset using a 1D transfer function based on scalar data values which is the most commonly used one (Figure 4.9 (A)). Then, the user can evaluate the result of the classification at the volume rendered image (Figure 4.9 (B)). If the user specified 1D transfer function is not sufficient to saliently visualize the interested features, the user can interact with the proposed transfer function using parallel coordinate (Figure 4.9 (C)). In practice, all the statistical and texture features are computed at the voxels which are selected by the user-specified 1D transfer function in order to reduce time complexity and improve classification accuracy. In the parallel coordinate, each parallel axis represents one of the statistical and texture feature (i.e., relative size, mean value, standard deviation, and texture features); and each voxel is represented as a polyline.

Figure 4.9 Data exploration based on multi-dimensional transfer function using parallel coordinates. (A) The user begins with classifying the volume dataset using a 1D transfer function based on scalar values. (B) The user can evaluate the result of the classification at the volume rendered image. (C) If the user specified 1D transfer function is not sufficient to saliently visualize the interested features, the user can interact with the proposed transfer function using parallel coordinates.

Figure 4.9 (C) shows the calculated statistical and texture features with green polylines. As the user selects the range on each axis, the parallel coordinate is highlighted by red polylines (red polylines in Figure 4.9 (C)); and 3D volume rendering is updated; selected

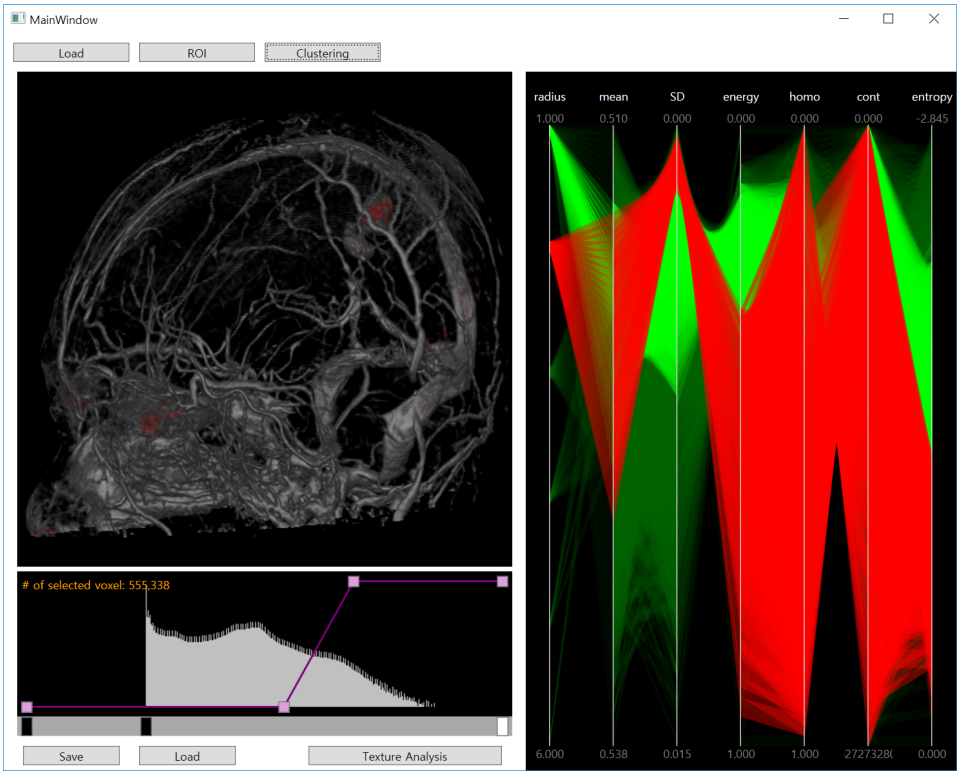

Figure 4.10 3D rendered image of brain tumor MR scans using automatic classification. Materials with similar intensities can be discriminated by the statistical and texture features. Highlighted polylines of parallel coordinate represent the brain tumor which is a dominant feature of $k-$means clustering with $k = 4$.

voxels are rendered with red color (Figure 4.9 (B)). This multi-dimensional transfer function design with parallel coordinates enables more interactive exploration of the transfer function space with multi-variate features.

Figure 4. 10 shows the 3D rendering of brain tumor MR scans. Using a 1D transfer function based on scalar data values, rendered

materials are depicted by the same color since they have similar intensities. However, the statistical (i.e., relative size, mean value, and standard deviation) and texture features (i.e., energy and entropy) of the tumor are different from the rest of the brain. Highlighted polylines of parallel coordinate represent the brain tumor.

Chapter 5. Conclusion

This paper proposes two approaches for the design of transfer functions. First, we propose a new 3D spatial field for effective visualization of constricted tubular structures, called as a stenosis map. It successfully discriminates constrictions within a tubular structure without laborious prior-segmentation of them. In the stenosis map, every voxel has a scalar value representing the degree of constriction relative to surrounding tubular structures. The degree of constriction is computed by newly proposed measures (i.e., line similarity measure and constriction measure) using the localized structure analysis based on the Hessian matrix and its eigenvalue signature. In addition, we have proposed a stenosis-based classification that maps the degree of constriction stored in the stenosis map to color and opacity. This classification provides easy and intuitive adjustment of the visual appearance of constrictions within tubular structures. We have explained the details of our method and its efficacy using an exemplary application to coronary artery stenoses. However, the proposed method can be directly applied to other constricted tubular structures only by the optimal selection of a few parameters. The performance evaluation using twenty-eight clinical datasets shows

that constricted regions are accurately encoded into the stenosis map and saliently visualized, demonstrating that our method can be an effective volume exploration tool in various, including but not limited to medicine, application fields of DVR.

Second, we propose a data exploration tool based on a new multi-dimensional transfer function using the statistical and texture features (i.e., relative size, mean value, standard deviation, and texture features), which employs parallel coordinates wherein each voxel is represented as a polyline with parallel axes of individual multi-dimensional features. This approach provides three specific ways to use our multi-dimensional transfer function based on parallel coordinates to enable the effective exploration of large and complex datasets. Using these ways of classification, it successfully discriminates different objects with the same intensities. Different texture features (e.g., homogeneity, contrast, and angular second moment) can be combined to classify various objects. We present a mechanism for data exploration with step-by-step illustration, demonstrating the practical efficacy of our proposed method. This multi-dimensional transfer function design with parallel coordinates enables more interactive exploration of the transfer function space with multi-variate features.

Bibliography

[1] W. E. Lorensen and H. E. Cline, "Marching cubes: A high resolution 3D surface construction algorithm," *ACM SIGGRAPH Comput. Graph.*, Vol. 21, No. 4, pp. 163-169, 1987.

[2] A. Knoll, Y. Hijazi, R. Westerteiger, M. Schott, C. Hansen, and H. Hagen, "Volume ray casting with peak finding and differential sampling," *IEEE Trans. Vis. Comput. Graph.*, Vol. 15, No. 6, pp. 1571-1578, 2009.

[3] K. Doi, "Computer-aided diagnosis in medical imaging: Historical review, current status, and future potential," *Comput. Med. Imag. Graph.*, Vol. 31, No. 4, pp. 198-211, 2007.

[4] B. V. Ginneken, C. M. Schaefer-Prokop, and M. Prokop, "Computer-aided diagnosis: How to move from the laboratory to the clinic," *Radiology*, Vol. 261, No. 3, pp. 719-732, 2011.

[5] M. Das *et al.*, "Small pulmonary nodules: Effect of two computer-aided detection systems on radiologist performance," *Radiology*, Vol. 241, No. 2, pp. 564-571, 2006.

[6] H. Chen, H. Li, Y. Fang, and Y. Chen, "Anisotropic parallel coordinates with adjustment based on distribution features," *J. Vis.*, Vol. 19, No. 2, pp. 327-335, 2016.

[7] A. Inselberg, "The plane with parallel coordinates," *Vis. Comput.*, Vol. 1, No. 2, pp. 69-91, 1985.

[8] A. Inselberg and B. Dimsdale, "Parallel coordinates: a tool for visualizing multi-dimensional geometry," In *Proc. IEEE Vis. 1990.*, pp. 361-378, 1990.

[9] J. Heinrich and D. Weiskopf, "State of the art of parallel coordinates," In *Proc. Eurographics 2013*, pp. 95-116, 2013.

[10] M. C. F. de Oliveira and H. Levkowitz, "From visual data exploration to visual data mining: A survey," *IEEE Trans. Vis. Comput. Graph.*, Vol. 9, No. 3, pp. 378-394, 2003.

[11] D. Mozaffarian *et al.*, "Heart disease and stroke statistics - 2015 update: A report from the american heart association," *Circulation*, Vol. 131, No. 1, pp. e29-e322, 2015.

[12] Z. Samad *et al.*, "A meta-analysis and systematic review of computed tomography angiography as a diagnostic triage tool for patients with chest pain presenting to the emergency department," *J. Nucl. Cardiol.*, Vol. 19, No. 2, pp. 364-376,

2012.

[13] U. Hoffmann *et al.*, "Coronary CT angiography versus standard evaluation in acute chest pain," *N. Engl. J. Med.*, Vol. 367, No. 4, pp. 299-308, 2012.

[14] K. A. Øvrehus, H. Munkholm, M. Bøttcher, H. E. Bøtker, and B. L. Nørgaard, "Coronary computed tomographic angiography in patients suspected of coronary artery disease: Impact of observer experience on diagnostic performance and interobserver reproducibility," *J. Cardiovasc. Comput. Tomogr.*, Vol. 4, No. 3, pp. 186-194, 2010.

[15] S. Cetin and G. Unal, "Automatic detection of coronary artery stenosis in CTA based on vessel intensity and geometric features," In *Proc. MICCAI Workshop 3D cardiovascular imaging: A MICCAI segmentation challenge*, 2012.

[16] C. D. Correa and K. L. Ma, "Size-based transfer functions: A new volume exploration technique," *IEEE Trans. Vis. Comput. Graph.*, Vol. 14, No. 6, pp. 1380-1387, 2008.

[17] C. D. Correa and K. L. Ma, "The occlusion spectrum for volume classification and visualization," *IEEE Trans. Vis. Comput. Graph.*, Vol. 15, No. 6, pp. 1465-1472, 2009.

[18] M. Haidacher, D. Patel, S. Bruckner, A. Kanitsar, and M.E. Gröller, "Volume visualization based on statistical transfer-function spaces," In *Proc. IEEE Pacific Vis. Symp.*, pp. 17-24, 2010.

[19] H. Hou, J. Sun, and J. Zhang, "Moment based transfer function design for volume rendering," In *Int. Conf. Grid Coop. Comput.*, pp. 215-218, 2003.

[20] J. S. Praßni, T. Ropinski, J. Mensmann, and K. Hinrichs, "Shape-based transfer functions for volume visualization," In *Proc. IEEE Pacific Vis. Symp.*, pp. 9-16, 2010.

[21] R. Wiemker, T. Klinder, M. Bergtholdt, K. Meetz, I. C. Carlsen, and T. Bülow, "A radial structure tensor and its use for shape-encoding medical visualization of tubular and nodular structures," *IEEE Trans. Vis. Comput. Graph.*, Vol. 19, No. 3, pp. 353-366, 2013.

[22] S. Bruckner, S. Grimm, A. Kanitsar, and M. E. Gröller, "Illustrative context-preserving exploration of volume data," *IEEE Trans. Vis. Comput. Graph.*, Vol. 12, No. 6, pp. 1559-1569, 2006.

[23] M. Levoy, "Display of surfaces from volume data," *IEEE Comput. Graph. Appl.*, Vol. 8, No. 3, pp. 29-37, 1988.

[24] G. Kindlmann and J. W. Durkin, "Semi-automatic generation of transfer functions for direct volume rendering," In *Proc. IEEE Symp. Vol. Vis.*, pp. 79-86, 1998.

[25] J. Hladůvka, A. König, and E. Gröller, "Curvature-based transfer functions for direct volume rendering," In *Spring Conf. Comput. Graph.*, Vol. 16, No. 5, pp. 58-65, 2000.

[26] G. Kindlmann, R. Whitaker, T. Tasdizen, and T. Möller, "Curvature-based transfer functions for direct volume rendering: Methods and applications," In *Proc. IEEE Vis. 2003.*, pp. 513-520, 2003.

[27] J. J. Caban and P. Rheingans, "Texture-based transfer functions for direct volume rendering," *IEEE Trans. Vis. Comput. Graph.*, Vol. 14, No. 6, pp. 1364-1371, 2008.

[28] J. Kniss, G. Kindlmann, and C. Hansen, "Multidimensional transfer functions for interactive volume rendering," *IEEE Trans. Vis. Comput. Graph.*, Vol. 8, No. 3, pp. 270-285, 2002.

[29] F. Y. Tzeng, E. B. Lum, and K. L. Ma, "An intelligent system approach to higher-dimensional classification of volume data," *IEEE Trans. Vis. Comput. Graph.*, Vol. 11, No. 3, pp. 273-284, 2005.

[30] S. Roettger, M. Bauer, and M. Stamminger, "Spatialized transfer functions," In *EuroVis*, pp. 271-278, 2005.

[31] R. Maciejewski, I. Woo, W. Chen, and D. S. Ebert, "Structuring feature space: A non-parametric method for volumetric transfer function generation," *IEEE Trans. Vis. Comput. Graph.*, Vol. 15, No. 6, pp. 1473-1480, 2009.

[32] D. Lesage, E. D. Angelini, I. Bloch, and G. Funka-Lea, "A review of 3D vessel lumen segmentation techniques: Models, features and extraction schemes," *Med. Image Anal.*, Vol. 13, No. 6, pp. 819-845, 2009.

[33] S. Wesarg, M. F. Khan, and E. A. Firle, "Localizing calcifications in cardiac CT data sets using a new vessel segmentation approach," *J. Digit. Imaging*, Vol. 19, No. 3, pp. 249-257, 2006.

[34] S. C. Saur, H. Alkadhi, L. Desbiolles, G. Székely, and P. C. Cattin, "Automatic detection of calcified coronary plaques in computed tomography data sets," In *Proc. Med. Image Comput. Comput. Assist. Interv.*, pp. 170-177, 2008.

[35] Y. Xu, G. Liang, G. Hu, Y. Yang, J. Geng, and P. K. Saha, "Quantification of coronary arterial stenoses in CTA using

fuzzy distance transform," *Comput. Med. Imaging Graph.*, Vol. 36, No. 1, pp. 11-24, 2012.

[36] Y. Yang, A. Tannenbaum, D. Giddens, and A. Stillman, "Automatic segmentation of coronary arteries using Bayesian driven implicit surfaces," In *Proc. 4th IEEE International Symposium on Biomedical Imaging*, pp. 189-192, 2007.

[37] S. Mittal *et al.*, "Fast automatic detection of calcified coronary lesions in 3D cardiac CT images," In *Proc. MICCAI Workshop on machine learning in medical imaging*, Vol. 6357, pp. 1-9, 2010.

[38] M. Teßmann, F. Vega-Higuera, D. Fritz, M. Scheuering, and G. Greiner, "Multi-scale feature extraction for learning-based classification of coronary artery stenosis," In *Proc. SPIE Med. Imaging*, Vol. 7260, pp. 726002-726002, 2009.

[39] M. A. Zuluaga, I. E. Magnin, M. H. Hoyos, E. J. F. D. Leyton, F. Lozano, and M. Orkisz, "Automatic detection of abnormal vascular cross-sections based on density level detection and support vector machines," *Int. J. Comput. Assist. Radiol. Surg.*, Vol. 6, No. 2, pp. 163-174, 2011.

[40] M. A. Zuluaga, D. Hush, E. J. F. D. Leyton, M. H. Hoyos, and M. Orkisz, "Learning from only positive and unlabeled data to

detect lesions in vascular CT images," In *Proc. Med. Image Comput. Comput. Assist. Interv.*, pp. 9-16, 2011.

[41] H. A. Kirişli *et al.*, "Standardized evaluation framework for evaluating coronary artery stenosis detection, stenosis quantification and lumen segmentation algorithms in computed tomography angiography," *Med. Image Anal.*, Vol. 17, No. 8, pp. 859-876, 2013.

[42] S. Potts, M. Tory, and T. Möller, "A Parallel coordinates interface for exploratory volume visualization," In *Proc. IEEE Vis. 2003.*, pp. 102, 2003.

[43] M. Tory, S. Potts, and T. Möller, "A Parallel Coordinates Style Interface for Exploratory Volume Visualization," *IEEE Trans. Vis. Comput. Graph.*, Vol. 11, No. 1, pp. 71-80, 2005.

[44] E. B. Lum, J. Shearer, and K. L. Ma, "Interactive multi-scale exploration for volume classification," *Vis. Comput.*, Vol. 22, No. 9, pp. 622-630, 2006.

[45] X. Zhao and A. Kaufman, "Multi-dimensional reduction and transfer function design using parallel coordinates," In *Proc. Int. Symp. Vol. Graph.*, pp. 69-76, 2010.

[46] J. Hladůvka, A. Konig, and E. Gröller, "Exploiting eigenvalues

of the hessian matrix for volume decimation," In *Proc. Int. Conf. Central Eur. Comput. Graph., Visual., Comput. Vis.*, pp. 124-129, 2001.

[47] Y. Sato *et al.*, "Tissue classification based on 3D local intensity structures for volume rendering," *IEEE Trans. Vis. Comput. Graph.*, Vol. 6, No. 2, pp. 160-180, 2000.

[48] J. Jin, L. Yang, X. Zhang, and M. Ding, "Vascular tree segmentation in medical images using hessian-based multiscale filtering and level set method," *Comput. Math. Methods Med.*, Vol. 2013, pp. 1-9, 2013.

[49] H. E. Bennink, H. C. van Assen, G. J. Streekstra, R. ter Wee, J. A. E. Spaan, and B. M. ter Haar Romeny, "A novel 3D multi-scale lineness filter for vessel detection," In *Proc. Med. Image Comput. Comput. Assist. Interv.*, pp. 436-443, 2007.

[50] K. Krissian, J. Ellsmere, K. Vosburgh, R. Kikinis, and C. F. Westin, "Multiscale segmentation of the aorta in 3D ultrasound images," In *Proc. 25th Annu. Int. Conf. IEEE Engineering in Medicine and Biology Society (EMBS)*, pp. 638-641, 2003.

[51] M. Rudzki, "Vessel detection method based on eigenvalues of the hessian matrix and its applicability to airway tree

segmentation," In *Proc. 11th international PhD Workshop OWD*, pp. 100-105, 2009.

[52] Q. Li, S. Sone, and K. Doi, "Selective enhancement filters for nodules, vessels, and airway walls in two- and three-dimensional CT scans," *Med. Phys.*, Vol. 30, No. 8, pp. 2040-2051, 2003.

[53] N. Funabashi, Y. Kobayashi, M. Perlroth, and G. D. Rubin, "Coronary artery: Quantitative evaluation of normal diameter determined with electron-beam CT compared with cine coronary angiography - Initial experience 1," *Radiology*, Vol. 226, No. 1, pp. 263-271, 2003.

[54] T. G. Flohr *et al.*, "Advances in cardiac imaging with 16-section CT systems," *Acad. Radiol.*, Vol. 10, No. 4, pp. 386-401, 2003.

[55] A. F. Frangi, W. J. Niessen, K. L. Vincken, and M. A. Viergever, "Multiscale vessel enhancement filtering," In *Proc. Med. Image Comput. Comput. Assist. Interv.*, pp. 130-137, 1998.

[56] E. A. Hulten, S. Carbonaro, S. P. Petrillo, J. D. Mitchell, and T. C. Villines, "Prognostic value of cardiac computed tomography angiography: A systematic review and meta-analysis," J. Am.

Coll. Cardiol., Vol. 57, No. 10, pp. 1237-1247, 2011.

[57] T. Porter and T. Duff, "Compositing digital images," *ACM SIGGRAPH Comput. Graph.*, Vol. 18, No. 3, pp. 253-259, 1984.

[58] E. K. Choi *et al.*, "Coronary computed tomography angiography as a screening tool for the detection of occult coronary artery disease in asymptomatic individuals," *J. Am. Coll. Cardiol.*, Vol. 52, No. 5, pp. 357-365, 2008.

[59] R. A. Drebin, L. Carpenter, and P. Hanrahan, "Volume rendering," *ACM SIGGRAPH Comput. Graph.*, Vo. 22, No. 4, pp. 65-74, 1988.

[60] M. Duval, E. Ouzeau, F. Precioso, and B. Matuszewski, "Coronary artery stenoses detection with random forest," In *Proc. MICCAI Workshop 3D cardiovascular imaging: a MICCAI segmentation challenge*, 2012.

[61] B. Mohr, S. Masood, and C. Plakas, "Accurate lumen segmentation and stenosis detection and quantification in coronary CTA," In *Proc. MICCAI Workshop 3D cardiovascular imaging: a MICCAI segmentation challenge*, 2012.

[62] R. Shahzad *et al.*, "Automatic segmentation, detection and quantification of coronary artery stenoses on CTA," *Int. J.*

Cardiovasc. Imaging, Vol. 29, No. 8, pp. 1847–1859, 2013.

[63] A. Broersen, P.H. Kitslaar, M. Frenay, and J. Dijkstra, "FrenchCoast: Fast, robust extraction for the nice challenge on coronary artery segmentation of the tree," In *Proc. MICCAI Workshop 3D cardiovascular imaging: a MICCAI segmentation challenge*, 2012.

[64] I. Öksüz, D. Ünay, and K. Kadıpaşaoğlu, "A hybrid method for coronary artery stenoses detection and quantification in CTA images," In *Proc. MICCAI Workshop 3D cardiovascular imaging: a MICCAI segmentation challenge*, 2012.

[65] I. Melki *et al.*, "Automatic coronary arteries stenoses detection in 3D CT angiography," In *Proc. MICCAI Workshop 3D cardiovascular imaging: a MICCAI segmentation challenge*, 2012.

[66] C. Wang, R. Moreno, Ö. Smedby, "Vessel segmentation using implicit model–guided level sets," In *Proc. MICCAI Workshop 3D cardiovascular imaging: a MICCAI segmentation challenge*, 2012.

[67] K. L. Lor and C. M. Chen, "Probabilistic model based evaluation of coronary artery stenosis on computed tomography angiography," In *Proc. MICCAI Workshop 3D*

cardiovascular imaging: a MICCAI segmentation challenge, 2012.

[68] A. Eslami *et al.*, "Quantification of coronary arterial stenosis by inflating tubes in CT angiographic images," In *Proc. MICCAI Workshop 3D cardiovascular imaging: a MICCAI segmentation challenge*, 2012.

[69] L. Flórez-Valencia *et al.*, "Coronary artery segmentation and stenosis quantification in CT images with use of a right generalized cylinder model," In *Proc. MICCAI Workshop 3D cardiovascular imaging: a MICCAI segmentation challenge*, 2012.

[70] C. M. Jarque and A. K. Bera, "Efficient tests for normality, homoscedasticity and serial independence of regression residuals," *Economics Letters*, Vol. 6, No. 3, pp. 255-259, 1980.

[71] B. L. Welch, "The generalization of student's problem when several different population variances are involved," *Biometrika*, Vol. 34, pp. 28-35, 1947.

[72] D. Gadkari, "Image quality analysis using GLCM," *University of Central Florida*, 2004.

[73] F. Albgretsen, "Statistical texture measures computed from

gray level cooccurrence matrices," *Image Processing Laboratory, Department of Informatics, University of Oslo*, pp. 1-14, 2008.

[74] R. M. Haralick, "Statistical and structural approaches to texture," In *Proc. IEEE*, Vol. 67, No. 5, pp. 786-804, 1979.

[75] M. Prokop and M. Galanski, "Spiral and multislice computed tomography of the body," *Thieme*, 2003.

초 록

직접 볼륨 렌더링(direct volume rendering, DVR)은 3차원 볼륨 데이터를 2차원 영상으로 재구성하는 가시화 기법 중 하나로, 볼륨 데이터에 색과 불투명도를 대응시키는 전이 함수(transfer function)를 이용한다. 직접 볼륨 렌더링에서 전이 함수는, 관심 영역은 강조하고 중요하지 않은 영역은 숨겨, 가시화의 품질에 큰 영향을 미치는 중요한 요소이다. 따라서 효과적인 가시화를 위한 전이 함수의 설계는 매우 중요하고 까다로운 과제이다. 본 논문에서는 관심 영역/특징을 정확히 식별하여 시각적으로 구별하기 위한 3차원 공간 필드와 다차원 전이 함수를 이용한 데이터 탐색 메커니즘을 제안한다.

먼저, 협착 관상 구조의 효과적인 가시화를 위해 3차원 공간 필드인 스테노시스맵(stenosis map)을 제안한다. 스테노시스맵은 주변 관상 구조에 비해 협착된 정도를 나타내는 스칼라 값을 저장하고 있으며, 이는 본 논문에서 새롭게 제안하는 국부적 구조 분석을 기반으로 한 측정 함수(선 유사도 측정 함수와 협착 측정 함수)에 의해 계산된다. 계산된 스테노시스맵은 협착 정도를 색과 불투명도에 대응시키는 전이 함수를 설계하는데 사용되어 협착 관상 구조를 효과적으로 가시화한다. 본 논문에서는 협착 관상 구조의 효과적인 가시화 기법을 관상 동맥 협착에 응용한 결과를 보여주며, 28개 임상 데이터의 성능 평가로 정확성과 효능을 입증한다.

둘째, 통계적으로 균질한 영역에서 계산된 질감 특성을 통합하는

새로운 다차원 전이 함수를 제안한다. 다차원 전이 함수 공간을 직관적으로 분석할 수 있도록 병렬 좌표계를 도입하고, 이를 사용하는 구체적인 세가지 방법을 제공하여 크고 복잡한 데이터를 효과적으로 탐색할 수 있도록 한다. 새로운 다차원 전이 함수를 이용한 데이터 탐색 메커니즘 제시하여, 제안된 방법의 실제적 효능을 입증한다.

본 논문은 직접 볼륨 렌더링의 전이 함수 설계에 관한 연구를 통해, 두 가지 유용한 기법을 제안한다. 협착 관상 구조의 효과적인 가시화 기법은 협착 관상 구조를 정확히 식별하여 시각적으로 구별할 뿐만 아니라 직관적인 사용자 인터페이스로 협착 관상 구조의 시각적 모양을 대화식으로 조정하여 관상 동맥 협착과 같은 방사선 진단에 상당한 도움을 준다. 또한 새로 설계한 다차원 전이 함수는 통계적으로 균질한 영역에서 계산된 질감 특징을 통합하고 병렬 좌표계를 이용한 직관적인 사용자 인터페이스를 제공하여 크고 복잡한 데이터를 직관적으로 탐색할 수 있는 강력한 도구이다.

주요어: 직접 볼륨 렌더링, 전이 함수, 관상 구조, 협착, 관상 동맥 협착, 병렬 좌표계

학 번: 2011-30246